Effect of stacking faults and surface roughness on the thermal conductivity of InAs nanowires

K. Vuttivorakulchai, M. Luisier, and A. Schenk

Citation: Journal of Applied Physics **124**, 205101 (2018); doi: 10.1063/1.5051677
View online: https://doi.org/10.1063/1.5051677
View Table of Contents: http://aip.scitation.org/toc/jap/124/20
Published by the American Institute of Physics

Effect of stacking faults and surface roughness on the thermal conductivity of InAs nanowires

K. Vuttivorakulchai,[a] M. Luisier,[b] and A. Schenk[c]
Integrated Systems Laboratory, ETH Zürich, Gloriastrasse 35, CH-8092 Zürich, Switzerland

(Received 10 August 2018; accepted 2 November 2018; published online 26 November 2018)

Low thermal conductivity and high power factor are desirable for thermoelectric materials. These properties can be achieved by patterning devices into nano-structures such as nanowires (NWs). The thermal conductivity can be further reduced by altering the NW geometry through the introduction of surface roughness (SR) or stacking faults (SFs). In this paper, relaxation times for scattering of phonons at SFs and SR are developed to accurately compute the impact of both effects on the thermal conductivity of InAs NWs with different diameters. It is found that similar reductions of the thermal conductivity can be obtained with SFs instead of SR. For the shortest possible distance between SFs along a NW, the room temperature thermal conductivity can be reduced to 25% compared to an ideal NW. For a NW with rough surface, a more than 80% decrease of the thermal conductivity is possible for specific roughness profiles. All available experimental data on the lattice thermal conductivity of InAs NWs confirm the theoretical models and simulation results. *Published by AIP Publishing.* https://doi.org/10.1063/1.5051677

I. INTRODUCTION

About two-thirds of the global energy production is lost as waste heat. Thermoelectric materials with a high ZT figure of merit are, therefore, long-desired to directly and reversibly convert heat back into usable electrical energy.[1] So far the highest ZT value, which is proportional to the power factor of the considered structure divided by its thermal conductivity, has been found in bulk SnSe. It could be attributed to its intrinsically ultra-low lattice thermal conductivity.[2] More conventional materials could also exhibit a high ZT value if they are patterned into nanostructures with a properly engineered surface. For instance, nanowires (NWs) with a rough surface have a higher ZT than their bulk counterparts due to their reduced lattice thermal conductivity.[3,4] An ultra-low lattice thermal conductivity can also result from the presence of stacking faults (SFs) intrinsic to NWs. The latter are naturally observed in III-V NWs, where zincblende (ZB) and wurtzite (WZ) crystal structures alternate (Fig. 1).[5]

Engineering the density of the SFs inside NWs may become an attractive design method for thermoelectric devices if the power factor term in ZT remains essentially unchanged or is not altered as much as the thermal conductivity. A high value of the power factor term can be obtained by (i) enhancing the Seebeck coefficient through a distortion of the electronic density of states (DOS), (ii) achieving high valley degeneracy by tuning the doping and composition or (iii) embedding nanocrystals in a thermoelectric material with further reducing the thermal conductivity.[6–13] Simulation and experiment have recently reported that the effect of electron-phonon interaction on phonon transport in samples with high doping concentration even reduces significantly the lattice thermal conductivity.[14,15] However, electron-phonon scattering is not included here because the conductivity model will be limited to the case of undoped InAs which also corresponds to the measurements by Karg *et al.*[5]

The distribution of the SFs can be controlled by tuning the growth parameters such as wire diameter, temperature, and doping concentration.[16,17] The optical and electrical properties of the material change as a function of the SF density. This offers opportunities for electronic band engineering and optoelectronic applications such as lasers, quantum-dot devices, and single-photon emitters for sensing, quantum information, and nano-photonics.[18–27] The focus of this paper is on properties like phonon dispersion, lattice thermal conductivity, phonon mean-free-path (MFP), and phonon lifetime in InAs NWs.

The situation is reversed in logic switches where silicon, the reference semiconductor, could be replaced in the near future by materials with better transport properties to give rise to transistors with enhanced performance (Fig. 1). This is the case of III-V materials (InGaAs), which are ideal for n-type applications due to their very high electron mobility.[28–30] However, it is not clear whether such materials can provide high enough thermal conductivities and thus minimize self-heating and the formation of local hot spots.[31] To shed light on this issue, the developed simulation model includes scattering of phonons at surface roughness (SR) and SFs and is applied to InAs NWs with diameters below 150 nm. This is the key to improve the figure of merit of thermoelectric generators based on III-V NWs or to minimize the impact of SR and SFs on the heat generation or evacuation in III-V logic switches.

The contributions from different scattering processes and phonon energy channels to the total thermal conductivity of bulk, ideal NWs, and non-ideal NWs with SFs and SR are analyzed. Predictions are made for modified NW structures that may open the door for new high-efficiency

[a]Electronic mail: kvuttivo@iis.ee.ethz.ch
[b]Electronic mail: mluisier@iis.ee.ethz.ch
[c]Electronic mail: schenk@iis.ee.ethz.ch

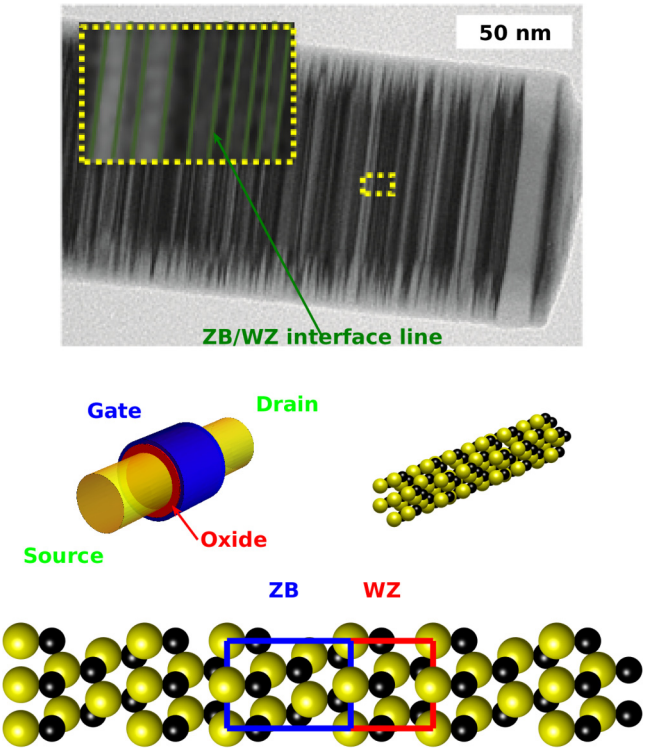

FIG. 1. Physical characterization of NWs with SFs. Top panel: Transmission electron micrograph of an InAs NW with SFs. From the zoom, one can extract the distance between the ZB/WZ interfaces. Bottom panel: Schematic view of a gate-all-around nanowire field-effect transistor and an atomic structure of the InAs NW with SFs. The blue box indicates the smallest unit cell forming a ZB lattice, while the red box refers to the WZ lattice.

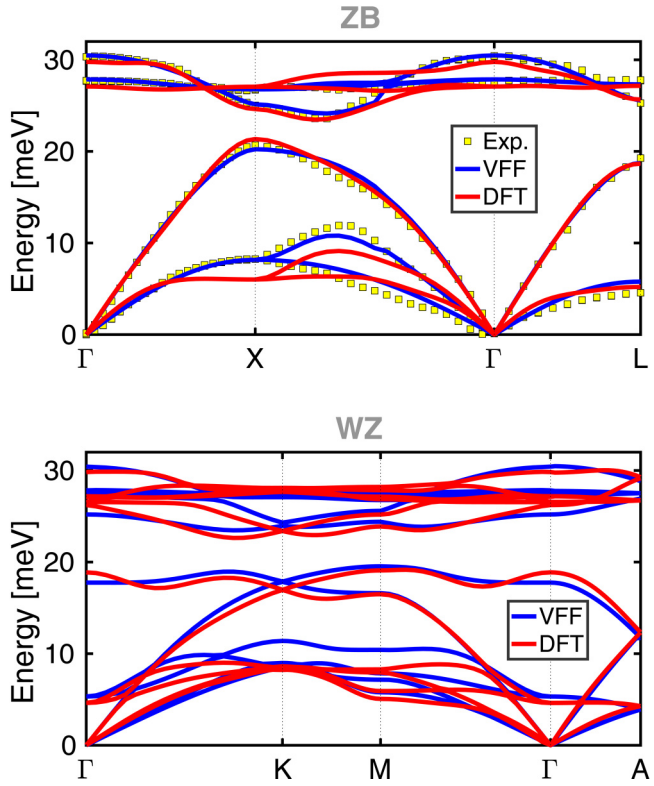

FIG. 2. Bulk phonon band structures of InAs with ZB and WZ lattices calculated by a VFF model and DFT. Circles represent experimental data.[35]

thermoelectric nano-devices that could be readily fabricated.[3,16,17,32]

II. THERMAL CONDUCTIVITY CALCULATION

Bulk InAs phonon dispersions of ZB and WZ structures calculated by a density-functional-theory (DFT) approach and a valence-force-field (VFF) model are shown in Fig. 2. The Vienna *ab initio* simulation package (VASP) was used for the DFT calculations.[33,34] The atomic Coulomb long-range potential which splits the transverse (TO) and longitudinal (LO) optical branches at the Γ-point and its vicinity is included in the calculation. The details of the simulation procedures can be found in Appendix A. Phonon bands calculated with the VFF model match the experimental data very well, whereas DFT calculations result in some deviations from both the measured acoustic and optical branches. For more accurate predictions of the thermal conductivity, the VFF model was chosen to produce the results outlined below.

The diffusive Landauer (*Ld*) formula is used to compute the thermal conductivity of bulk and NW structures[36]

$$k_{ph}(\mathrm{T}) = \frac{1}{A}\int \Xi(\omega)\lambda_{ph}^{Ld}(\omega, \mathrm{T})\frac{\hbar\omega}{2\pi}\frac{\partial n_0}{\partial \mathrm{T}}d\omega. \quad (1)$$

From the bulk band structure, the number of states crossing a given frequency can be extracted to obtain the number of modes $\Xi(\omega)$ at a given phonon frequency ω. Here, T is the lattice temperature, A is the cross-sectional area of the conductor, and n_0 is the Bose-Einstein distribution function. The Landauer (or phonon) mean-free-path (MFP) for backscattering $\lambda_{ph}^{Ld}(\omega, \mathrm{T})$ is 4/3 times longer than the common MFP $[\lambda_{ph}(\omega, \mathrm{T}) = v_{ph}(\omega)\tau_{ph}(\omega, \mathrm{T})]$ in the three-dimensional $\boldsymbol{q}$-space, where $v_{ph}(\omega)$ is the average phonon group velocity at a given frequency.[37] Each scattering mechanism is described by a relaxation time (RT) [partial phonon lifetime $\tau_\alpha(\omega, \mathrm{T})$]. The total scattering rate $\tau_{ph}^{-1}(\omega, \mathrm{T})$ is obtained by summing the inverse partial RTs of all involved scattering processes. Apart from scattering at SFs and SR, anharmonic phonon-phonon scattering (only Umklapp processes) $[\tau_{anh}^{-1}(\omega, \mathrm{T}) = B\omega^2\mathrm{T}e^{-C/\mathrm{T}}]$, scattering at defects from isotope mass variations $[\tau_{def}^{-1}(\omega) = P\omega^4]$, and crystalline boundary scattering $[\tau_b^{-1}(\omega) = v_{ph}(\omega)/l_b]$ are taken into account. The crystalline boundary scattering MFP (l_b) is often used as fitting parameter to model the transition from bulk to narrow NWs. The schematics of NW geometries with SFs and SR as well as the different scattering mechanisms are illustrated in Fig. 3. SR scattering can be diffusive [short phonon wavelengths comparable to the asperity height (Δ)] or specular (phonon wavelength much longer than Δ).[38]

Large computational efforts are required to calculate the phonon bands of NWs with diameters larger than 50 nm. An alternative way is to rely on bulk properties to estimate the NW ones.[36] As in bulk phonon band structure calculations and in a previously proposed approach, cubic unit cells are extracted from the NWs.[36] The orientations of these unit cells are changed according to the NW growth directions, ⟨111⟩ for ZB and ⟨0001⟩ for WZ. The full-band phonon dispersions are computed from these unit cells. The transport direction is aligned with the x-axis in all cases. The wave vector $\boldsymbol{q}$ in

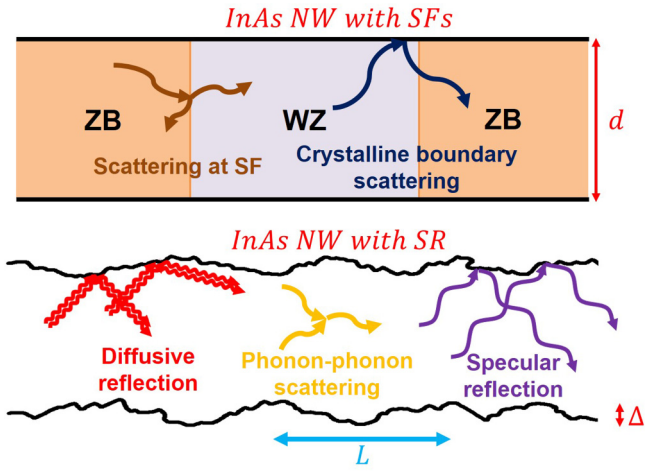

FIG. 3. Phonon scattering mechanisms. Top panel: An InAs NW with SFs. Bottom panel: An InAs NW with SR.

the first Brillouin zone (BZ) of both structures is discretized by 401 points along the transport direction and 101 in the others. $\Xi(\omega)$ and $v_{ph}(\omega)$ can then be obtained from these ballistic phonon bands along the x-axis. The phonon density-of-states (DOS) and $v_{ph}(\omega)$ of the ZB and WZ structures are shown in Fig. 4. Small differences between the ZB and WZ DOS can be observed. The perturbation operator needed for the relaxation time of SF scattering is assumed to be proportional to the difference ΔV of the bulk ZB and WZ phonon band structures integrated over the first BZ and summed over all branches. However, the bulk band structures of Fig. 2 cannot be directly used because the

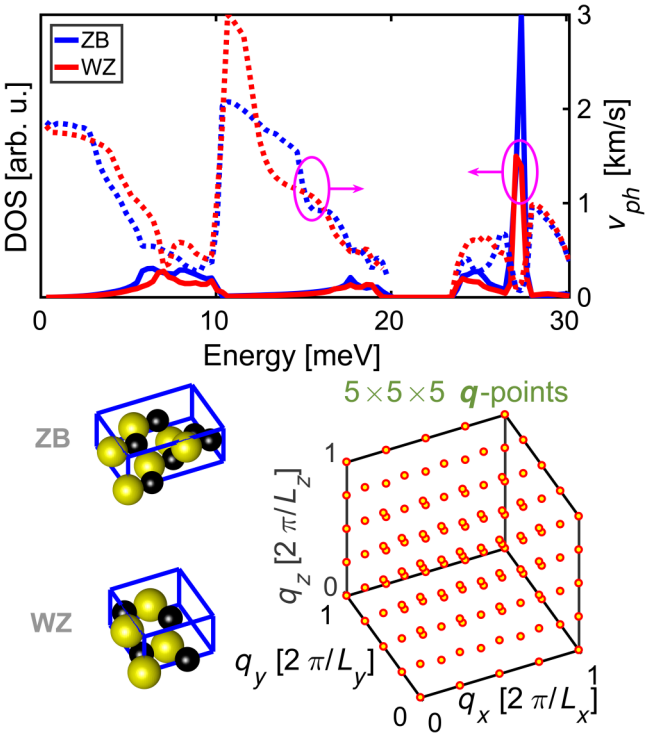

FIG. 4. Top panel: Phonon DOS (solid lines) and $v_{ph}(\omega)$ (dotted lines) of the ZB (blue color) and WZ (red color) phases. Bottom panel: The corresponding unit cell structures of ZB and WZ and an example of $5 \times 5 \times 5$ $\boldsymbol{q}$-point sampling in the first BZ.

number of bands and the unit cells are different. The bulk phonon bands of a ZB, ZB-WZ super-lattice (SL), and WZ structure with equal number of bands and computed with the same unit cells (hexagonal structure) are presented in Appendix A. Despite the close resemblance of the ZB-WZ, ZB, and WZ band structures, the measured thermal conductivity of InAs nanowires with stacking faults is much smaller than in ideal nanowires.[5] Thus, in this paper, the interface scattering at stacking faults is treated in the relaxation time approximation using the difference between the ZB and WZ phonon bands as perturbation.

Figure 5 shows ΔV as a function of phonon energy. The number of atoms in the unit cells of ZB and WZ was chosen such that the number of bands becomes equal. The form of the two (three) cubic unit cells along the x-axis of the ZB (WZ) structure was adapted accordingly. The first Brillouin zone (BZ) was discretized as described in the above procedure. The overall average of the energy difference is about 0.14 meV (0.21 meV) as a result of the VFF (DFT) calculation. Note that ΔV has a maximum of about 2 meV at a phonon energy of ~20 meV in the DFT case. This can also be seen in Appendix A.

For the modeling of the scattering processes, the only difference between bulk and NW is the boundary scattering due to geometrical confinement in the NW. In NWs, the parameter l_b is equal to the nanowire diameter (d) multiplied by a factor F which accounts for the uncertainty of the measured diameter. Note that the parameter l_b will be used in the following. The parameters B, C, and l_b are derived by fitting the thermal conductivity to experimental data of bulk-like InAs samples, while P is analytically determined from the isotope mass variations[39,40]

$$P = \frac{V_a}{2\pi v_s^3}\left[\left(\frac{\bar{M}_{In}}{\bar{M}_{In}+\bar{M}_{As}}\right)^2 g_{In} + \left(\frac{\bar{M}_{As}}{\bar{M}_{In}+\bar{M}_{As}}\right)^2 g_{As}\right], \quad (2)$$

where V_a is the atomic volume, v_s is the average sound velocity, and g is the phonon scattering parameter of the mass fluctuation made up of several isotopes for a single element

$$g = \sum_m f_m \left(\frac{M_m - \bar{M}}{\bar{M}}\right). \quad (3)$$

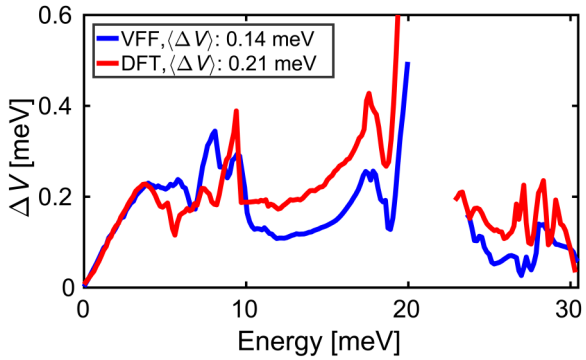

FIG. 5. Energy difference between ZB and WZ phonon band structures as a function of phonon energy.

In this expression, f_m is the atomic fraction of the mth isotope whose mass is M_m and $\bar{M}$ is the average mass of different isotopes from the same atomic element. The parameters B, C, P, and l_b (bulk InAs) are equal to 2.3×10^{-19} s/K, 59 K, 2.7×10^{-45} s^3, and 2.8 mm, respectively. No further parameter is required to predict the thermal conductivity of the NW.

The ZB and WZ crystal structures give almost the same bulk lattice thermal conductivity which fits well to the experimental data (Fig. 6). The thermal conductivity of a NW is calculated here by adjusting the crystalline boundary scattering to the NW geometry. Note that, due to the conical shape,[44] the diameter varies along the wire. The average of the values at the two ends was chosen to determine the parameter l_b. The factor F was then fitted to the measured thermal conductivity of the NWs. The calculated results show good agreement to currently available measured values in the diameter range from ~60 nm to ~150 nm in the case of InAs NWs (Fig. 6). SFs and SR can be directly added to the picture through the inverse phonon RT they induce.

A. Imperfect boundary scattering

First-order perturbation theory requires a proper perturbation operator describing the lattice distortions. In the general case of imperfect boundary scattering, phonons experience different potential heights and widths along a NW (see Fig. 7). The one-dimensional model for such a chain of non-equidistant potential barriers with varying width and height results in an inverse RT $1/\tau_{bs}$ of the form (see the derivation in Appendix B)

$$\frac{1}{\tau_{bs}(\omega)} = \frac{\sum_n \Delta V_n^2 w_n^2 \mathrm{si}^2(q_x w_n)}{v_x(\omega)\hbar^2 \sum_n (l_n + w_n)}, \tag{4}$$

where w_n is the potential width at x_n (n is up to the total number of scattering boundaries, N), l_n is the local distance between two barriers, $v_x(\omega)$ is the phonon group velocity in x-direction at a given phonon energy, ΔV_n is the height of the potential barrier at x_n, $\mathrm{si}(x) = \sin(x)/x$, and $\omega = \omega(q_x)$. Note that non-diagonal terms $\sim \Delta V_n \Delta V_{n'}$ do not occur for random l_{sf} and in the limit $N \to \infty$ (see Appendix B), and Eq. (4) can be applied to any boundary type such as grain, line, dislocation, and SFs.

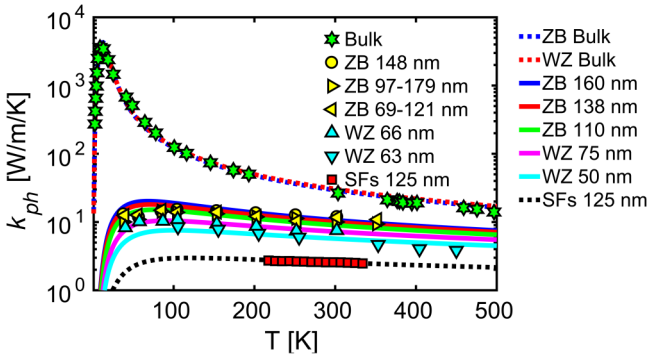

FIG. 6. Thermal conductivity of InAs as a function of T for bulk, ideal NWs, NWs with SFs of ZB and WZ structures. Numbers inside (outside) the figure obtained from the literature[5,41–44] (from our calculations) are represented by d (l_b). The symbols refer to experimental data.[5,41–44]

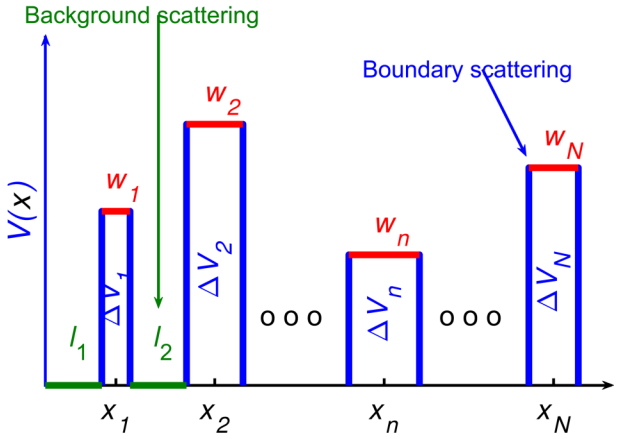

FIG. 7. Model potential for boundary and background scatterings.

Under the assumption $w_n \ll l_n$ for all n, one can use the limits $w_n = w \to 0$ and $\Delta V_n = \Delta V$ which lead to (see Appendix B)

$$\frac{1}{\tau_{sf}(\omega)} = \frac{v_x(\omega)}{l_{sf}} \frac{1 - T_{sf}}{T_{sf}}. \tag{5}$$

Here, l_{sf} is the average distance between SFs and T_{sf} is the phonon transmission coefficient of the SF. For electron scattering at grain boundaries (GBs), the same form of the RT was first given by Mayadas *et al.*[45] Serov *et al.* adapted this expression to the scattering of phonons at GBs.[46] If l_{sf} can be extracted from experiments, the phonon transmission coefficient T_{sf} is the only fitting parameter. The underlying assumption is that phonons are scattered at an ultra-thin potential barrier induced by the SF, neglecting the differences between ZB and WZ phonon properties. An alternative way is to directly use Eq. (4) and apply the obvious replacements $l_n + w_n = 2l_{sf}$, $\Delta V_n = \Delta V$. This results in (see Appendix B)

$$\frac{1}{\tau_{sf}(\omega)} = \frac{\Delta V^2}{2\hbar^2 l_{sf} v_x(\omega)} \frac{1}{N} \sum_n w_n^2 \mathrm{si}^2(q_x w_n), \tag{6}$$

where ΔV is now the fitting parameter. Its value can be either validated by or directly used from the calculated difference between the ZB and WZ phonon band structures. Assuming an exponential distribution of w_n, the inverse RT becomes (see Appendix B)

$$\frac{1}{\tau_{sf}(\omega)} = \frac{l_{sf}\Delta V^2}{\hbar^2 v_x(\omega)\left[1 + 4q_x^2 l_{sf}^2\right]}. \tag{7}$$

The thermal conductivity of NWs with $d \approx 125$ nm that have a dense distribution of SFs with l_{sf} in-between 2 nm and 3 nm (Fig. 1) was measured by Karg *et al.*[5] Based on these samples, $l_{sf} \approx 2.5$ nm has been chosen for the simulations.

The fitting parameter $\Delta V = 0.21$ meV with $l_{sf} = 2.5$ nm was found to produce a good fit to the experimental data, as shown in Fig. 8 (black dotted line). After fitting the model parameters, the thermal conductivity of structures with various distributions of l_{sf}, including the case of a superlattice, can be predicted. The period of the latter covers one

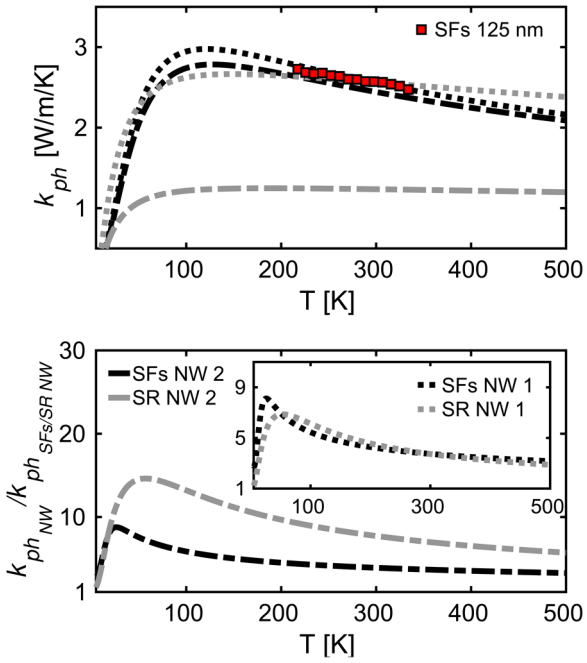

FIG. 8. Top panel: Calculated thermal conductivity of InAs NWs with SFs ($l_b = 125$ nm), $l_{sf} = 2.5$ nm (black dotted line, SFs NW 1), and $l_{sf} = 0.87$ nm (black dashed-dotted line, SFs NW 2) and of NWs with SR ($\Delta = 4.4$ nm, gray dotted line, SR NW 1 and $\Delta = 7.6$ nm, gray dashed-dotted line, SR NW 2) for $L = 6$ nm. The symbols represent experimental data.[5] Bottom panel: Ratio of the thermal conductivity of an ideal NW ($l_b = 125$ nm) to the thermal conductivity of corresponding NWs with SFs or SR (SFs NW 1 in the inset, SR NW 1 in the inset, SFs NW 2, and SR NW 2).

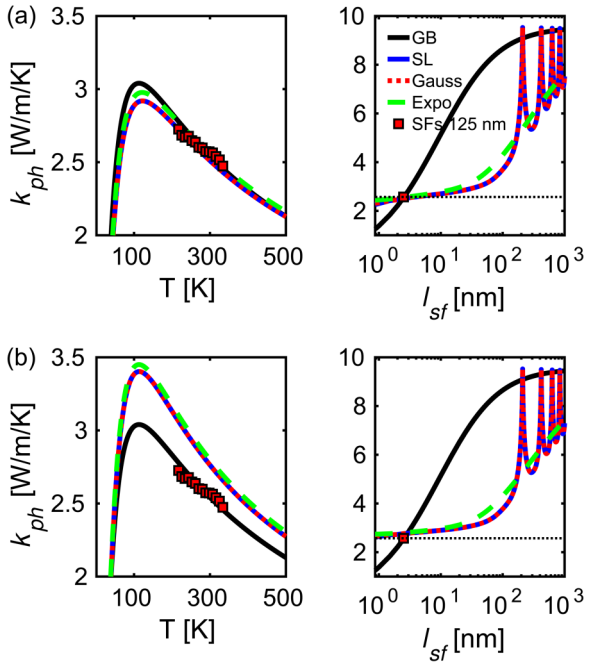

FIG. 9. Thermal conductivity of SFs NWs with different l_{sf}-distributions ($\sigma = 0.5$ nm for Gaussian distribution) as function of T and in comparison to the grain-boundary model of Eq. (5) ($T_{sf} = 0.72$) at $l_{sf} = 2.5$ nm (left) and T = 300 K (right). (a) With a fixed $\Delta V = 0.21$ meV. (b) With ΔV from the direct calculation of the energy difference between ZB and WZ structures, as shown in Fig. 5 for the VFF model. The black thin dotted line indicates the experimental value of the thermal conductivity at 300 K. Experimental data (red squares) are from Karg *et al.*[5]

wire unit cell of ZB and one wire unit cell of WZ (Fig. 1) and has the value $l_{sf} \approx 0.87$ nm. The corresponding result for the thermal conductivity is shown in Fig. 8 (black dashed-dotted line). In the long-wavelength limit, all distributions result in the same expression for the inverse RT

$$\frac{1}{\tau_{sf}(\omega)} = \alpha \frac{l_{sf}\Delta V^2}{\hbar^2 v_x(\omega)} \tag{8}$$

with a numerical pre-factor α which has the following values: 1 for exponential (Expo); 1/2 for super-lattice (SL), Poisson, and sharp Gaussian (Gauss); and 2/3 for the uniform distribution. The general expressions for all l_{sf} distributions can be found in Appendix B. In the short-wavelength limit, the inverse RT is

$$\frac{1}{\tau_{sf}(\omega)} = \alpha' \frac{\Delta V^2}{2\hbar^2 v_x(\omega) l_{sf} q_x^2} \tag{9}$$

with $\alpha' = 1$ for SL, sharp Gaussian, and uniform distributions, as well as 1/2 for exponential distribution.

Figure 9 presents the calculated thermal conductivities based on the inverse RT of different SF distributions. In Fig. 9(a), ΔV was fixed to 0.21 meV. All l_{sf}-distributions such as SL, Gauss, and Expo result in equally good fits to the experimental data. The inverse RT of grain-boundary scattering according to the model provided by Serov *et al.*, Eq. (5), was used with the fitted value of $T_{sf} = 0.72$ for all T and l_{sf}. The corresponding thermal conductivity for this case is shown by the black curve in Fig. 9. For small values of l_{sf}, it falls short of the other distributions. The unphysical periodicity of the thermal conductivity in the cases of SL and Gauss for large $l_{sf} > 200$ nm originates from the si-function. However, the above-quoted limit $N \to \infty$ excludes such long distances between SFs. The pre-factor in the case of the exponential distribution in Eq. (8) is larger than in the SL and Gauss cases (by 2 in the long-wavelength limit). The opposite behavior is found in the short-wavelength limit. The numerical calculations take into account all possible values between the short- and long-wavelength limits. Interestingly, the integration over all wavelengths results in very similar thermal conductivities. In Fig. 9(b), the calculated difference between ZB and WZ band structures as a function of phonon energy is used (see Fig. 5 for the VFF model). The corresponding conductivity values then exceed the experimental data by 5%–10%. It is possible that there are some other unknown factors that further reduce the thermal conductivity, thus explaining this difference. The value $\Delta V = 0.21$ meV fitted to the experimental data will be kept for the following analysis. Note that this value is exactly the average difference between ZB and WZ phonon bands obtained by the DFT approach.

B. Surface roughness scattering

First-order perturbation theory (Fermi's golden rule) is also employed to derive the RT of SR scattering. With two parameters, the root-mean-square value of the roughness fluctuations (Δ) and its autocorrelation length (L), the surface of

rough NWs can be fully characterized. The geometrical parameters of a rough InAs NW are illustrated in the bottom panel of Fig. 3. The anharmonic potential related to a dilatation is chosen as perturbation operator (see the derivation in Appendix C). The total phonon scattering rate for a phonon branch p is the sum of the phonon scattering rates over all branches p'. The final expression for the SR scattering RT becomes

$$\frac{1}{\tau_{sr}^{\boldsymbol{q},p}} = \frac{\omega_{\boldsymbol{q},p}^2 \gamma^2 \Delta^2 L^2}{4\pi d} \times \sum_{p'} \int_{\omega_{\boldsymbol{q}',p'}=\omega_{\boldsymbol{q},p}} \frac{dS'}{v_{ph}(\omega_{\boldsymbol{q}',p'})} e^{-|\boldsymbol{q}'-\boldsymbol{q}|^2 L^2/4} \delta_{q_z'-q_z,0}, \quad (10)$$

where γ is the Grüneisen parameter (0.57 for InAs)[47] and dS' is the surface element of the $\boldsymbol{q}$-integration domain. Above formula holds for a Gaussian autocorrelation (GA) function for the SR. The case of an exponential autocorrelation (EA) function is presented in Appendix C.

A GA function will be considered in the following analysis. For the results presented in Fig. 8, Δ was set to 4.4 nm at $L = 6$ nm in order to obtain the same reduction of the thermal conductivity as predicted in the case where SFs dominate (gray dotted line). A further 50% reduction of the thermal conductivity in SR NWs could be obtained by setting $\Delta = 7.6$ nm and $L = 6$ nm (gray dashed-dotted line in Fig. 8). However, a NW of 125 nm in diameter with this roughness configuration could not be easily manufacturable. To achieve an ultra-low thermal conductivity of ~ 1.4 W/m/K, a narrower NW with $d = 60$ nm, $\Delta = 4$ nm, and $L = 5$ nm would be needed. This is because the SR scattering rate is inversely proportional to the NW diameter as expressed in Eq. (10). Such NWs have been already produced with Si by Lim *et al.*[32]

The ratios of the thermal conductivity of ideal NWs to those with SFs or SR are plotted in Fig. 8. At room temperature, the thermal conductivity is reduced to about 25% at $l_{sf} < 2.5$ nm for the SFs case or $\Delta = 4.4$ nm, $L = 6$ nm for the SR case and by about 12.5% at $\Delta = 7.6$ nm, $L = 6$ nm. These ratios behave differently in that the ratio for the SFs (SR) case is always larger than 1 (approaches 1) in the limit $T \to 0$. The same behavior was also found in previous calculations of the thermal conductivity of Si NWs with SR.[48]

III. SCATTERING CONTRIBUTIONS

In this section, the significance of each scattering mechanism contributing to the total thermal conductivity will be presented and discussed in detail. In NWs with dominant SF scattering, the phonon MFP and the thermal conductivity are reduced at all temperatures, as seen in Figs. 10(a) and 10(b). This is a reason why the ratio of ideal NW to SFs NW in Fig. 8 is larger than 1 in the limit $T \to 0$. At very low temperatures ($T < 20$ K), boundary scattering has the strongest effect on the nanowires with dominant SR scattering, whereas in the high-temperature range for both cases a decaying trend for the temperature dependence of MFP and thermal conductivity caused by phonon-phonon Umklapp scattering can be observed [see Figs. 10(a) and 10(b)]. Umklapp processes are more dominant in bulk than in ideal NWs at high temperatures, whereas the crystalline boundary scattering becomes more important at low temperatures. The turning point temperature of the ideal InAs NW with $d = 125$ nm where the dominant scattering process changes from crystalline boundary to phonon-phonon scattering is about 270 K. The turning point temperature rises with decreasing diameter which lowers the MFP of the crystalline boundary scattering. Point-defect or impurity scattering has the least impact on total MFP and lattice thermal conductivity.

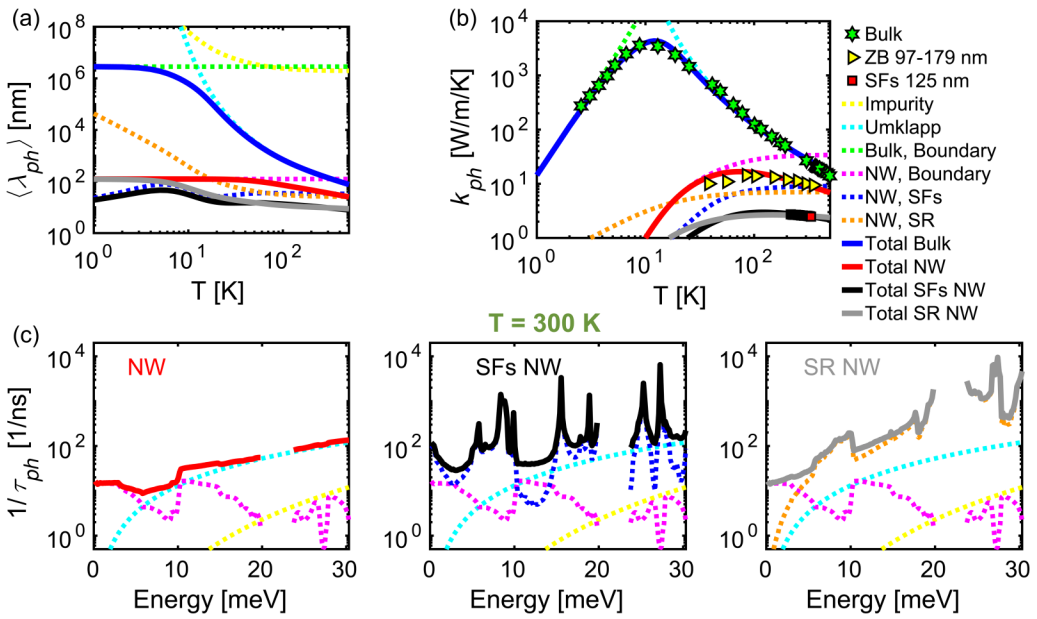

FIG. 10. Contributions from different scattering processes for bulk, ideal NW, NW with SFs ($l_{sf} = 2.5$ nm), and NW with SR ($\Delta = 4.4$ nm, $L = 6$ nm). For all NWs, $l_b = 125$ nm. (a) Phonon MFP as a function of T. (b) Thermal conductivity as a function of T. The contribution from impurity scattering is far outside the plotting range. Symbols refer to experimental data.[5,41–44] (c) Scattering rates of ideal NW, NW with SFs, and NW with SR as a function of phonon energy at room temperature.

The scattering rates for an ideal NW at room temperature in Fig. 10(c) reveal that crystalline boundary scattering is the strongest mechanism at phonon energies below 6 meV. Above this energy, Umklapp scattering dominates. For the NW with SFs ($l_{sf} = 2.5$ nm), the SF scattering rate is larger than all the others over most of the energy range. The sharp peaks correspond to very small group velocities in the transport direction according to Eq. (7). The slower the phonons propagate in the transport direction, the more it is scattered by the ZB/WZ potential barriers. For a SR with $\Delta = 4.4$ nm and $L = 6$ nm, SR scattering dominates almost everywhere except at very low energies (LE) where crystalline boundary scattering is stronger.

Figure 11 illustrates the temperature-dependent contribution of the different energy intervals to the total thermal conductivity. Low energies (LE), intermediate energies (IE), and high energies (HE) are defined here as the energy channels ranging from 0 to 10 meV (mainly populated by the transverse acoustic branches), from 10 to 20 meV, and from 20 meV to the maximum phonon energy, respectively. LE phonons have the biggest share over the whole temperature range except for the SFs cases. The effect of geometrical confinement reduces the contribution by the LE phonons and enhances the contribution of IE phonons.

A higher SF density (black dotted lines in Fig. 11) has the effect that the contribution from SF scattering increases in the IE and HE intervals. Its scattering rate dominates in the entire energy range as seen in Fig. 10(c), and the rate becomes even stronger when l_{sf} decreases. This results in a smaller contribution in the LE region while the contributions in the IE and HE intervals increase. The behavior is different in the SR case. The SR scattering rate depends on the square of the phonon energy. In the IE and HE intervals, the main contribution comes from the SR scattering, while in the LE interval, the contribution from boundary scattering becomes equally important when $\omega \to 0$ and cannot be neglected [see Fig. 10(c)]. When Δ increases, SR scattering in the LE interval has a weaker influence on the increase of the scattering rate compared to the IE and HE intervals. Thus, the LE region yields the main contribution to the total thermal conductivity.

In the diffusive limit, the lattice thermal conductivity in Eq. (1) can be written as[37]

$$k_{ph}(\mathrm{T}) = \frac{1}{A} K_{bal}(\mathrm{T}) \left\langle \lambda_{ph}^{Ld}(\mathrm{T}) \right\rangle \tag{11}$$

with K_{bal} the ballistic thermal conductance

$$K_{bal}(\mathrm{T}) = \frac{k_B^2 \mathrm{T} \pi^2}{3h} \int \Xi_{ph}(\omega) W_{ph}(\omega, \mathrm{T}) d(\hbar\omega) \tag{12}$$

and W_{ph} the window function given by

$$W_{ph}(\omega, \mathrm{T}) = -\frac{3(\hbar\omega)^2}{(\pi k_B \mathrm{T})^2} \frac{\partial n_0}{\partial(\hbar\omega)}. \tag{13}$$

The quantum of the thermal conductance is the factor in front of the integral of Eq. (12), and the average Landauer phonon MFP for back scattering at a given T can be derived as[37]

$$\left\langle \lambda_{ph}^{Ld}(\mathrm{T}) \right\rangle = \frac{\int \Xi(\omega) \lambda_{ph}^{Ld}(\omega, \mathrm{T}) W_{ph}(\omega, \mathrm{T}) d(\hbar\omega)}{\int \Xi(\omega) W_{ph}(\omega, \mathrm{T})\, d(\hbar\omega)} = \frac{4}{3} \left\langle \lambda_{ph}(\mathrm{T}) \right\rangle. \tag{14}$$

The integral of the window function over all energies is equal to 1. The phonon energies relevant for the thermal conduction can be described by W_{ph}. At room temperature, W_{ph} is almost constant, i.e., the whole phonon energy range is equally important. At lower temperature, LE phonons are favored, whereas HE phonons of InAs have small group velocities (Fig. 4) and, therefore, their weight for the total phonon RT becomes negligible. More details on the energy and temperature dependence of W_{ph} can be found in Appendix D.

At very low temperatures, the LE phonons are always the major contributors to the thermal conductivity because the window function is mostly confined in this LE channel. HE phonons are always the least important. For NWs with SR, the contribution from the HE interval can even be lower than in the case of bulk InAs (Fig. 11). The design of thermoelectric nano-devices would greatly benefit from the suppression of those energy channels that mainly contribute to the thermal conductivity.

IV. THERMAL CONDUCTIVITY PREDICTION

The phonon band structure, lattice thermal conductivity, phonon MFP, and phonon lifetime in bulk InAs and NWs calculated and discussed in Secs. II and III are in good agreement with available experimental data. This now

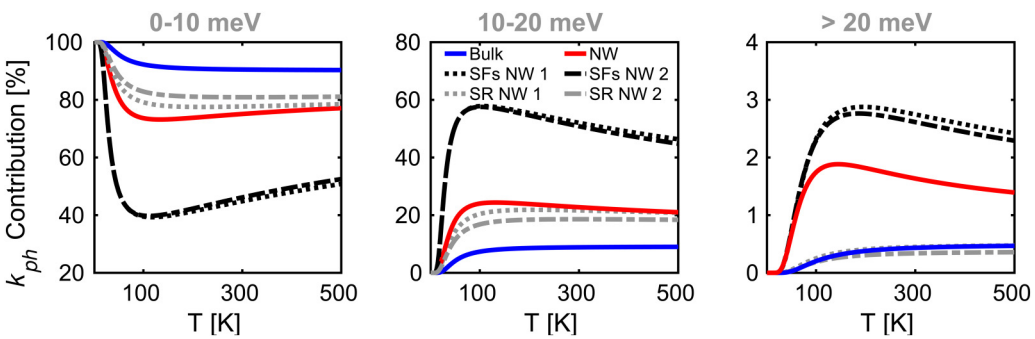

FIG. 11. Contribution of different energy intervals to the total thermal conductivity (0-10 meV, 10-20 meV, and >20 meV) for bulk, ideal NW, NW with SFs 1 (2) with $l_{sf} = 2.5$ nm ($l_{sf} = 10$ nm), and NW with SR 1 (2) with $\Delta = 4.4$ nm and $L = 6$ nm ($\Delta = 7.6$ nm and $L = 6$ nm). For all NWs, $l_b = 125$ nm.

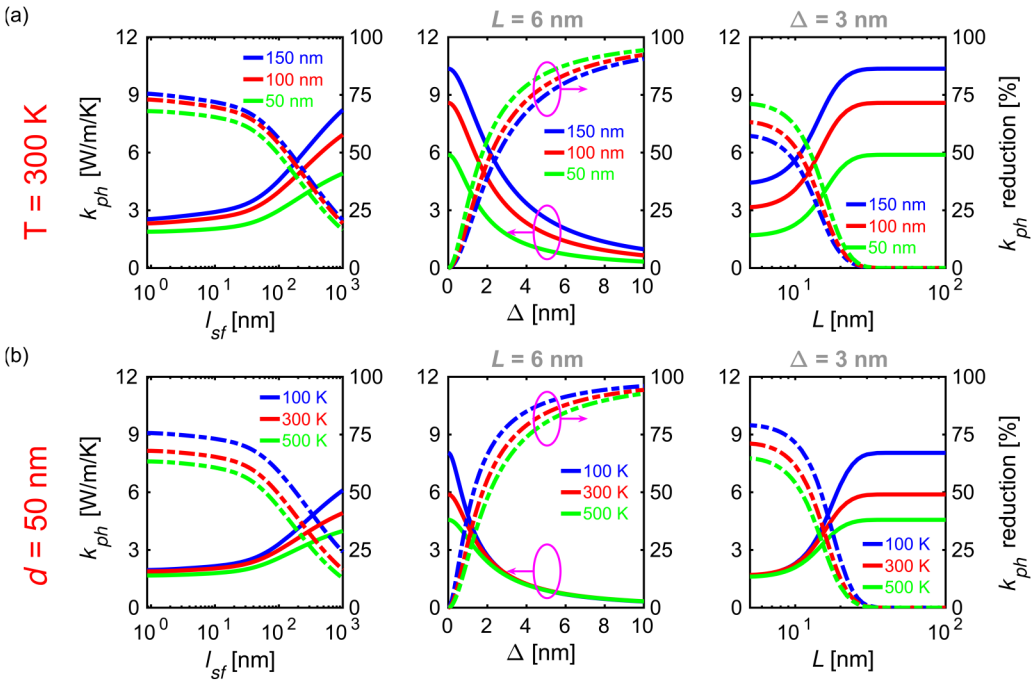

FIG. 12. Thermal conductivity (solid lines) and its relative reduction (dashed-dotted lines) with respect to ideal NWs as a function of the model parameters l_{sf}, L, and Δ. (a) NW diameter variation at 300 K. Numbers in figures are the values of l_b. (b) Temperature variation for a diameter of 50 nm. Numbers in figures are the temperature.

allows us to make predictions where experimental studies have not yet been conducted.

Temperature and NW diameter variations are shown in Fig. 12. They have a decreasing impact on the thermal conductivity when the SFs are denser packed, because scattering at SFs becomes the dominant process. A distance $l_{sf} > 1\,\mu$m is sufficient to prevent a large reduction of the NW thermal conductivity and, therefore, suppresses self-heating and the eventual degradation of InAs-based logic switches. Experimentally observed, the most frequent distance is $l_{sf} \approx 10$ nm, which can decrease the thermal conductivity by about 70% at room temperature, even more at low temperatures. It halves itself compared to an ideal NW at $l_{sf} \approx 100$ nm. Here, the non-diagonal terms $\sim \Delta V_n \Delta V_{n'}$ were neglected. Diameter scaling slightly reduces the contribution of SF scattering to the total thermal conductivity [Fig. 12(a)], i.e., transistors with very narrow InAs channels would be least affected.

With decreasing temperature, the proportionate reduction of the thermal conductivity increases in all cases, as shown in Fig. 12(b). The temperature dependence of the thermal conductivity almost disappears when l_{sf} decreases, Δ increases at fixed L, and L decreases at fixed Δ, respectively. With increasing surface-to-volume ratio, the proportionate reduction of the thermal conductivity in an ideal NW becomes larger. Unlike in the case of dominant SF scattering, acoustic phonons in the LE interval are only influenced by the confinement perpendicular to the x-direction. The RT of SR scattering [see Eq. (10)] is inversely proportional to the diameter of the NW which offers the possibility to reduce the thermal conductivity significantly by reducing the cross section. Aspects of self-heating and thermal degradation of InAs-NW-based switches are the same as in the case of SF scattering. Independent of temperature and diameter, the thermal conductivity increases when L exceeds ~5 nm and becomes constant when $L \approx 30$ nm as shown in Fig. 12. The same increase can be observed in the measured thermal conductivity of the Si NWs with SR.[32] Decreasing temperature and increasing diameter accelerate the rise of the thermal conductivity when L increases. NWs with small L are difficult to fabricate. A minimum value of $L \approx 5$ nm can be observed in Lim *et al.*[32]

V. CONCLUSION

In summary, the presented simulations of the thermal conductivity of InAs NWs agree well with all existing experimental data. In order to prevent a reduction of the thermal conductivity by at least 80%, the distance l_{sf} between SFs must be greater than 1 μm, the roughness amplitude Δ must be very small, and the autocorrelation length L large. The highest possible density of SFs in a NW with 125 nm in diameter gives rise to a 75% decrease of the thermal conductivity compared to an ideal NW at room temperature and a 50% reduction at $l_{sf} \approx 100$ nm. At low temperatures, the decrease can be >75%. A 70% reduction would occur in 125 nm NWs with engineered rough surface when $\Delta = 3$ nm at $L = 6$ nm. In order to achieve a very low thermal conductivity of a realistic NW (~1.4 W/m/K), parameters should be similar to $\Delta = 4$ nm, $L = 5$ nm, and $d = 60$ nm which were already demonstrated by Lim *et al.* for Si NWs.[32] The SR has a stronger effect when the NW diameter is scaled down, in contrast to scattering at SFs. The simulations also prove the principal possibility of engineering an ultra-low lattice thermal conductivity of InAs NWs to achieve a high ZT provided the power factor term in ZT is not altered as much as the thermal conductivity.

ACKNOWLEDGMENTS

The authors gratefully acknowledge funding from the Swiss National Science Foundation through SNF under project 149454 (TORNAD) and Bernd Gotsmann, Heinz Schmid, and Siegfried Karg (IBM-Research Zürich) for useful discussion.

APPENDIX A: PHONON BAND STRUCTURE OF INAS

InAs phonon dispersions of ZB, WZ, and SFs structures will be first analyzed in this section. Two methods of phonon band calculations are used and compared here.

(i) First-principles calculations based on projector augmented-wave (PAW) pseudopotentials[49] for the electron-ion interactions from Blöchl[50] and the local-density approximation (LDA) as implemented in VASP[33,34] were performed. The PAW pseudopotentials were chosen such that the [Kr] $4d^{10}$ ([Ar] $3d^{10}$) electrons of In (As) are considered according to a frozen core approximation. A $2 \times 2 \times 2$ Monkhorst-Pack $\boldsymbol{k}$-point grid according to 1 $\boldsymbol{k}$-point in the irreducible wedge of the BZ was used.[51] The partial occupancies for each wave function were set by the Gaussian smearing method with 50 meV smearing width of an energy cutoff of 400 eV. For the electronic self-consistency loop, the convergence criteria of 10^{-8} eV/A force acting on each ion and a total energy difference of 10^{-8} eV between two subsequent iterations were employed to assure highly converged forces. The eight-atom cubic cell of InAs was located at (0, 0, 0), (0, 0.5, 0.5), (0.5, 0, 0.5), and (0.5, 0.5, 0) for In and (0.25, 0.25, 0.25), (0.25, 0.75, 0.75), (0.75, 0.25, 0.75), and (0.75, 0.75, 0.25) for As. Supercells of 216 atoms ($3 \times 3 \times 3$ conventional cells) were used to evaluate the harmonic interatomic force-constants (IFCs) (Hessian) matrix via density functional perturbation theory (DFPT). Phonon bands were then computed by employing the Hessian matrix.

(ii) A modified VFF model was used to compute the short-range interaction potential of InAs, which depends solely on atomic positions.[52] Five types of short-range interactions can accurately capture the bulk InAs phonon dispersions. The total short-range interaction potential is then given by

$$\begin{aligned} U = & \sum_i \sum_{j\in NN(i)} \frac{\alpha_{ij}}{b_{ij}^2}\left(\boldsymbol{r}_{ij}^2 - \boldsymbol{b}_{ij}^2\right)^2 \\ & + \sum_i \sum_{j\in NN(i)} \sum_{\substack{k\in NN(i)\\ k\neq j}} \frac{\beta_{jik}}{b_{ij}b_{ik}}\left(\boldsymbol{r}_{ij}\cdot\boldsymbol{r}_{ik} - \boldsymbol{b}_{ij}\cdot\boldsymbol{b}_{ik}\right)^2 \\ & + \sum_i \sum_{j\in NN(i)} \sum_{\substack{k\in NN(i)\\ k\neq j}} \frac{\zeta_{jik}}{b_{ij}b_{ik}}\left(\boldsymbol{r}_{ij}^2 - \boldsymbol{b}_{ij}^2\right) \\ & \times \left(\boldsymbol{r}_{ij}\cdot\boldsymbol{r}_{ik} - \boldsymbol{b}_{ij}\cdot\boldsymbol{b}_{ik}\right) \\ & + \sum_i \sum_{j\in NN(i)} \sum_{\substack{k\in NN(i)\\ k\neq j}} \frac{\chi_{jik}}{b_{ij}b_{ik}}\left(\boldsymbol{r}_{ij}^2 - \boldsymbol{b}_{ij}^2\right)\left(\boldsymbol{r}_{ik}^2 - \boldsymbol{b}_{ik}^2\right) \\ & + \sum_i \sum_{j\in NN(i)} \sum_{\substack{k\in NN(i)\\ k\neq j}} \sum_{\substack{l\in NN(k)\\ l\neq i}}^{COP} \frac{\kappa_{jikl}}{\sqrt{b_{ij}b_{ik}b_{ki}b_{kl}}} \\ & \times \left(\boldsymbol{r}_{ij}\cdot\boldsymbol{r}_{ik} - \boldsymbol{b}_{ij}\cdot\boldsymbol{b}_{ik}\right)\left(\boldsymbol{r}_{ki}\cdot\boldsymbol{r}_{kl} - \boldsymbol{b}_{ki}\cdot\boldsymbol{b}_{kl}\right), \end{aligned} \tag{A1}$$

where $\boldsymbol{r}_{ij} = \boldsymbol{r}_j - \boldsymbol{r}_i$ is the bond vector from atom i to j and $\boldsymbol{b}_{ij}$ is the equilibrium bond vector connecting atoms i and j. The variables $NN(i)$ and COP denote the nearest neighbors of atom i and the plane formed by the coplanar atoms i, j, k, and l, respectively. The potential parameters (α, β, ζ, χ, and κ) are short-range force constants corresponding to bond stretching, bond bending, stretch-bend interactions, cross-stretch interactions, and coplanar bend-bend interactions, respectively. To obtain the phonon band structure, the stationary phonon equation of motion must be solved. This equation can be written as an eigenvalue problem

$$\sum_{\sigma,\eta'} D_{\rho,\sigma}(\eta\eta'|\boldsymbol{q}) w_{n\sigma}(\eta'|\boldsymbol{q}) = \omega_n^2(\boldsymbol{q}) w_{n\rho}(\eta|\boldsymbol{q}), \tag{A2}$$

where η and η' are atom indices inside the structure unit cell, while ρ and σ refer to Cartesian coordinates. The quantities ω_n and $w_{n\rho}$ represent the phonon frequencies and eigenvectors, respectively, for phonon branch n and phonon wave vector $\boldsymbol{q}$. The dynamical matrix of the considered atomic structure (D) is the summation of the short-range (sr) and long-range (lr) interaction components, where the contribution from the short-range interaction potential is defined as

$$\begin{aligned} D_{\rho,\sigma}^{sr}(\eta\eta'|\boldsymbol{q}) = & \frac{1}{\sqrt{M_\eta M_{\eta'}}} \\ & \times \sum_{l',l=0} \Phi_{\rho,\sigma}(l\eta|l'\eta') e^{-i\boldsymbol{q}\cdot[\boldsymbol{r}(l\eta)-\boldsymbol{r}(l'\eta')]}. \end{aligned} \tag{A3}$$

Here, M is the atom mass and l' is the unit cell index of the whole atomic structure. The atomic matrix of the force constants (Φ) at the atomic equilibrium positions ($\boldsymbol{R}$) is calculated as

$$\Phi_{\rho,\sigma}(i|j) = \left.\frac{\partial^2 U}{\partial r_{i\rho}\partial r_{j\sigma}}\right|_{\boldsymbol{R}}, \tag{A4}$$

with the potential U given in Eq. (A1).

Coulomb interactions build the long-range potential. This effect must be properly accounted for in the phonon band calculation in order to correctly model the splitting of the TO and LO branches at the Γ-point and its vicinity, as observed experimentally (Fig. 2). The background dielectric screening of the Coulomb interaction is integrated into the effective point charge (Q_i) of atom i.[53] The Coulomb interactions between the ions can be written as

$$U_{Coul} = \frac{1}{4\pi\varepsilon_0} \sum_{i<j} \frac{Q_i Q_j}{|\boldsymbol{r}_i - \boldsymbol{r}_j|}. \tag{A5}$$

The most popular method to include the Coulomb interactions while simulating the phonon band structure is through Ewald summation.[54] However, this approach is computationally very demanding since the summation over a large number of reciprocal lattice vectors must be performed to ensure a converged phonon band structure. Hence, more efficient methods have been developed to

TABLE I. Five VFF potential parameters (α, β, ζ, χ, and κ) in units of N/m, Born effective charge tensor ($\underline{Z}^*$), and a free parameter (Ψ) of 8.79 nm^{-1} for VFF and 2.59 nm^{-1} for DFT. The dielectric tensor ($\underline{\varepsilon}$) is equal to $12.3 \times I_3$, where I_3 is the identity matrix with size 3.

	α	β	ζ	χ	κ	$\underline{Z}^*$
In	34.01	3.04	−0.79	3.02	0.47	$2.50 \times I_3$
As	34.01	3.04	−0.79	3.02	0.47	$-2.50 \times I_3$

include Coulomb interactions. A rough sketch of one of the methods is given in the following paragraph.

A faster evaluation of the Coulomb potential can be done by avoiding the summation over the reciprocal lattice vectors as suggested by Parlinski *et al.*[55] The main idea here consists in modifying the expression from Parlinski *et al.* and adding it directly to the long-range component of the dynamical matrix, which then can be rewritten as

$$D^{lr}_{\rho,\sigma}(\eta\eta'|\boldsymbol{q}) = \frac{4\pi q_e^2}{\Omega\sqrt{M_\eta M_{\eta'}}} \frac{\left[\boldsymbol{q}\cdot\underline{Z}^*_{\eta}\right]_\rho \left[\boldsymbol{q}\cdot\underline{Z}^*_{\eta'}\right]_\sigma}{\boldsymbol{q}\cdot\underline{\varepsilon}\cdot\boldsymbol{q}^t} e^{-|\boldsymbol{q}|^2/\Psi^2}, \quad \text{(A6)}$$

where q_e is the elementary charge, $\boldsymbol{q}^t$ is the transpose of the phonon wave vector, $\underline{Z}^*$ is the Born effective charge tensor, $\underline{\varepsilon}$ is the high-frequency static dielectric tensor, Ω is the volume of the primitive unit cell, and Ψ is a free parameter that suppresses the influences of this long-range dynamical matrix and includes the effect of the phase-factor difference in atomic positions.

Figure 2 shows the bulk InAs phonon dispersions of ZB and WZ structures calculated by a DFT approach and a VFF model. The atomic Coulomb long-range potential which splits the TO and LO branches at the Γ-point and its vicinity is included in the calculation. The VFF parameters are summarized in Table I. Phonon bands calculated with the VFF model match the experimental data very well, whereas DFT calculations result in some deviations from both the measured acoustic and optical branches. To avoid inaccurate predictions of the thermal conductivity, the VFF model was chosen to produce the results in the other sections.

To be able to compare the band structures of bulk ZB, super-lattice of ZB and WZ (ZBWZ), and WZ lattices, the number of atoms in the unit cells of all structures must be equal. The corresponding unit cells are shown in Fig. 13(a). These structures are fully relaxed with LDA. Figure 13(b) presents the corresponding band structures based on the VFF and DFT calculations, respectively.

Figure 14 shows the shifted band energies (ΔV) among these 3 different structures [presented in Fig. 13(a)] and their band counting. A $\boldsymbol{q}$-sampling with 401 points along the x-axis and 101 points in the other two directions of the reciprocal lattice was chosen. The energy differences ZBWZ-ZB and WZ-ZBWZ computed by the VFF method are similar to those from the DFT method. The ZBWZ band energy is about in the middle of the other two, but all band counts are very similar. A strong shift in the band energy appears at ∼20 meV [see Fig. 14(b)], where the maximum values are ∼1.4 meV for WZ-ZBWZ and ∼1.7 meV for WZ-ZB.

APPENDIX B: SCATTERING OF PHONONS AT STACKING FAULTS

Perturbation theory is employed to calculate the perturbing Hamiltonian caused by lattice distortions. To derive RT for scattering at SFs, the general case of imperfect boundary scattering with varying potential heights (ΔV_n) and widths (w_n) of N boundaries along the NW x-axis will be considered first (see Fig. 7). The perturbing potential with

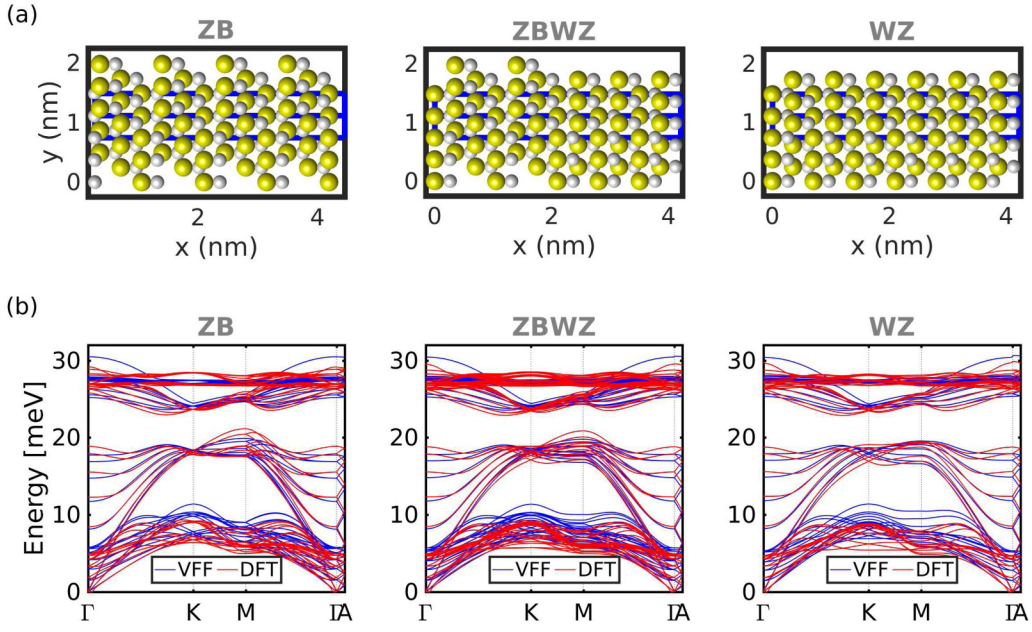

FIG. 13. Comparison of bulk ZB, ZBWZ, and WZ lattices. (a) Hexagonal structures along the ⟨111⟩ direction of ZB and the ⟨0001⟩ direction of WZ. The blue solid lines are unit cells used for the computation of bulk band structures with the same number of atoms in each cell. (b) Corresponding bulk band structures of ZB, ZBWZ, and WZ.

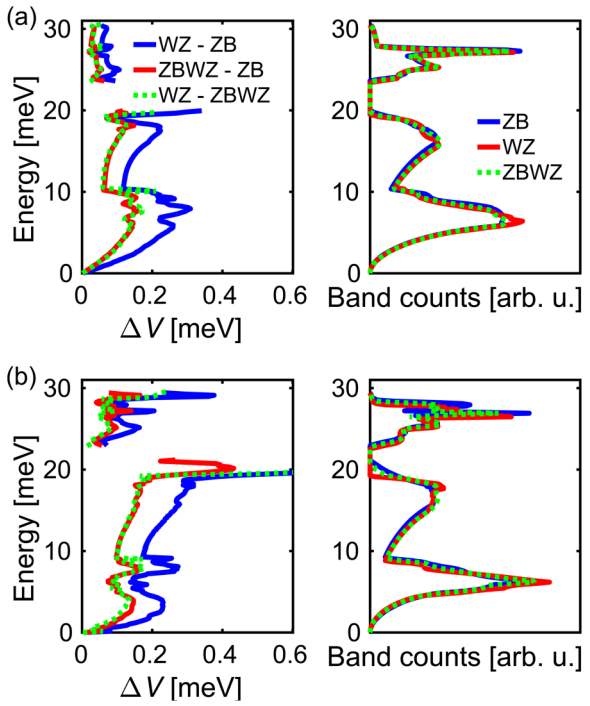

FIG. 14. Band energy differences among ZB, WZ, and ZBWZ structures and their band counts. (a) VFF calculation. (b) DFT calculation. Band energy of WZ (ZBWZ, WZ) differs from ZB (ZB, ZBWZ) represented by WZ-ZB (ZBWZ-ZB, WZ-ZBWZ), respectively.

height (ΔV_n) represents the energy shifted between phonon band structures of the two phases (ZB and WZ) present in segments w_n, whereas the segments with width l_n are those of the ideal (unperturbed) NW (either ZB or WZ). Using rectangular functions rect(u) of variable u, the whole potential profile can be modeled as sum of the individual perturbation potentials

$$V(x) = \sum_{n}^{N} \Delta V_n \mathrm{rect}\left(\frac{x - x_n}{w_n}\right). \tag{B1}$$

Fermi's golden rule is used to determine the transition probability from the initial state with momentum $\boldsymbol{q}$ and energy $\hbar\omega$ to the final state with momentum $\boldsymbol{q}'$ and energy $\hbar\omega'$ per unit time t due to a perturbing Hamiltonian H'. It is given by

$$\wp(\boldsymbol{q}, p; \boldsymbol{q}', p') = \frac{2\pi}{\hbar^2} |\langle \boldsymbol{q}, p|H'|\boldsymbol{q}', p'\rangle|^2 \delta\left(\omega_{\boldsymbol{q},p} - \omega_{\boldsymbol{q}',p'}\right). \tag{B2}$$

In order to obtain the total transition rate, summation over all modes $\boldsymbol{q}'$ is required. The volume $\boldsymbol{q}$-space summation can be transformed to a surface integral over dS'. Total phonon scattering rate of a phonon branch p is the sum of the phonon scattering rates over all branches p'

$$\frac{1}{\tau} = \frac{2\pi}{\hbar^2} \sum_{p'} \frac{V}{(2\pi)^3} \int \frac{dS'}{v_{ph}\left(\omega_{\boldsymbol{q}',p'}\right)} d\omega_{\boldsymbol{q}',p'} \times |\langle \boldsymbol{q}, p|H'|\boldsymbol{q}', p'\rangle|^2 \delta\left(\omega_{\boldsymbol{q}',p'} - \omega_{\boldsymbol{q},p}\right), \tag{B3}$$

where V is the volume of the simulated device and $v_{ph}(\omega)$ is the phonon group velocity for a given phonon energy. Using the plane wave expansion, the phonon wave function can be written as

$$\langle \boldsymbol{r}|\boldsymbol{q}', p'\rangle = \frac{1}{V} e^{i\boldsymbol{q}'\cdot\boldsymbol{r}}. \tag{B4}$$

The square of the transition matrix element can be decomposed as

$$|\langle \boldsymbol{q}, p|H'|\boldsymbol{q}', p'\rangle|^2 = H_{ind}^2 + H_{int}^2, \tag{B5}$$

where the diagonal term (H_{ind}) is given by

$$H_{ind}^2 = \frac{1}{L_x^2} \sum_{n=n'}^{N} \Delta V_n^2 w_n^2 \times \mathrm{si}^2\left[\left(q_x' - q_x\right) \cdot w_n/2\right] \delta\left(\boldsymbol{q}_\rho' - \boldsymbol{q}_\rho\right). \tag{B6}$$

Here, L_x is the length of the NW, $\delta(\boldsymbol{q}_\rho' - \boldsymbol{q}_\rho)$ is the Kronecker delta of the component of $\boldsymbol{q}$ in the yz-plane, and $\mathrm{si}(x) = \sin(x)/x$ is the si-function The off-diagonal term (H_{int}), describing scattering by two different potential barriers, reads

$$H_{int}^2 = \frac{1}{L_x^2} \sum_{n\neq n'}^{N} \Delta V_n w_n \mathrm{si}\left[\left(q_x' - q_x\right) \cdot w_n/2\right] \times \Delta V_{n'} w_{n'} \mathrm{si}\left[\left(q_x' - q_x\right) \cdot w_{n'}/2\right] \times e^{-i\left(q_x' - q_x\right)\cdot\left(x_{n'} - x_n\right)} \delta\left(\boldsymbol{q}_\rho' - \boldsymbol{q}_\rho\right). \tag{B7}$$

The inverse RT in Eq. (B3) can then be obtained as the sum

$$\frac{1}{\tau} = \frac{1}{\tau_{ind}} + \frac{1}{\tau_{int}}, \tag{B8}$$

where the diagonal part τ_{ind}^{-1} from all boundaries (i.e., barriers) is given by

$$\frac{1}{\tau_{ind}} = \frac{1}{N\langle l_n + w_n\rangle v_x \hbar^2} \sum_{n=1}^{N} \Delta V_n^2 w_n^2 \mathrm{si}^2(q_x w_n) \tag{B9}$$

and the off-diagonal part τ_{int}^{-1} from the interaction with two different boundaries (barriers) by

$$\frac{1}{\tau_{int}} = \frac{1}{N\langle l_n + w_n\rangle v_x \hbar^2} \times \sum_{n,n'\neq n}^{N} \Delta V_n w_n \Delta V_{n'} w_{n'} \times \mathrm{si}(q_x w_n) \mathrm{si}(q_x w_{n'}) e^{2iq_x\left(x_{n'} - x_n\right)}. \tag{B10}$$

In Eqs. (B9) and (B10), v_x is the x-component of the phonon group velocity, and the angular brackets denote the average $\langle f_n\rangle = \frac{1}{N}\sum_1^N f_n$. As the off-diagonal term vanishes in the limit $N \to \infty$ and for a random distribution of w_n, it will be skipped. Therefore, Eq. (B9) is the final form for the rate τ_{bs} of phonon scattering at imperfect boundaries

$$\frac{1}{\tau_{bs}(\omega)} = \frac{1}{N\langle l_n + w_n\rangle v_x \hbar^2} \sum_{n=1}^{N} \Delta V_n^2 w_n^2 \mathrm{si}^2(q_x w_n). \tag{B11}$$

This expression is general and can be applied to grain, line, and dislocation scattering as well as scattering at SFs.

The RT for SR scattering will be derived in a different way in Appendix C. In the case of grain boundary (GB) scattering, the limit $w_n = w \to 0$ leads to

$$\frac{1}{\tau_{GB}(\omega)} = \frac{v_x(\omega)}{l_{GB}} \frac{1 - T_{GB}}{T_{GB}} \tag{B12}$$

(l_{GB} denotes the average grain size). This equation having the same form as in Serov *et al.*[46] immediately follows from Eq. (B11) under the assumption

$$\Delta V^2 w_{GB}^2 = v_x^2 \hbar^2 \left(\frac{1 - T_{GB}}{T_{GB}} \right), \tag{B13}$$

which can be derived from the textbook formula for the transmission T of a plane wave through a thin ($q_x w_n \ll 1$) rectangular barrier. Equation (5) is the same as Eq. (B12), with *GB* replaced by *sf*.

In the case of SF scattering, the potential barrier is caused by the phonon band structures of two different phases of the same material. Therefore, all potential heights ΔV_n have the same value ΔV. The actual distribution of the w_n after growth is not known; hence, all standard models are considered for completeness in the following. We compute the RT for a super-lattice $[\delta(w_n - l_{sf})]$, exponential $[\exp(-w_n/l_{sf})/l_{sf}]$, Gaussian $\{1/\sqrt{2\pi\sigma^2}\exp[-(w_n - l_{sf})^2/2\sigma^2]\}$, uniform $(1/L_x)$, and Poisson $[(l_{sf}/a)^n \exp(-l_{sf}/a)/n!]$ distribution, respectively, where a is the lattice constant and $|l_{sf} - l_{sf,min}| \gg \sigma$ is assumed. The summary of the resulting inverse RTs τ_{sf}^{-1} is

$$\frac{1}{\tau_{sf}(\omega)} = \begin{cases} \frac{l_{sf}\Delta V^2}{2\hbar^2 v_x(\omega)} \mathrm{si}^2(q_x l_{sf}), \\ \frac{l_{sf}\Delta V^2}{\hbar^2 v_x(\omega)\left[1+4q_x^2 l_{sf}^2\right]}, \\ \frac{l_{sf}\Delta V^2}{4\hbar^2 v_x(\omega)} \mathrm{si}^2(q_x l_{sf}) \left[1 + \mathrm{erf}\left(\frac{l_{sf}}{\sqrt{2\sigma^2}}\right)\right], \\ \frac{\Delta V^2}{4\hbar^2 v_x(\omega) l_{sf} q_x^2} [1 - \mathrm{si}(2q_x L_x)], \\ \frac{\Delta V^2 e^{-l_{sf}/a}}{2\hbar^2 v_x(\omega) l_{sf}} \sum_{n=0}^{N} a^2 n^2 \mathrm{si}^2(q_x a n) \left(\frac{l_{sf}}{a}\right)^n \frac{1}{n!}, \end{cases} \tag{B14}$$

respectively. Here, l_{sf} is the average distance between two consecutive SFs and $\mathrm{erf}(u)$ is the error function of variable u.

APPENDIX C: SURFACE ROUGHNESS SCATTERING

A RT for phonon SR scattering has been given by Martin *et al.*[48] and in our previous study.[36] Below, an improved derivation will be presented in detail, which is similar to that of Klemens for the perturbation energy matrix element due to a static strain field.[56] However, our calculation of the RT due to a dilatation explicitly treats the exact anharmonic potential caused by this dilatation as perturbing Hamiltonian. The NW geometry is then applied to surface profiles of Gaussian and exponential autocorrelations (GA and EA) for the SR. The SR profiles are described in the common way by Δ and L.

The dynamics of an elastic continuum is considered here instead of the lattice dynamics because it allows to link macroscopic quantities like the Grüneisen parameter (γ) associated with the thermal expansion phenomenon to the interatomic force constants and anharmonicity. Ziman[38] presented this theory in a formalism that parallels, as completely as possible, the dynamics of a lattice. The total energy consists of the potential energy density as quadratic function of the local strain ($\partial\boldsymbol{\eta}/\partial\boldsymbol{r}$), the kinetic energy of the motion described by a momentum variable $\boldsymbol{p}(\boldsymbol{r})$, and the anharmonic potential energy

$$\begin{aligned} \mathcal{H} = & \frac{1}{2}\int d\boldsymbol{r} \sum_{\alpha\beta\gamma\delta} \frac{\partial\eta_\alpha}{\partial r_\beta}\frac{\partial\eta_\gamma}{\partial r_\delta} G_{\alpha\gamma}^{\beta\delta} + \frac{1}{2}\int d\boldsymbol{r} \mathfrak{D}_0^{-1} \boldsymbol{p}(\boldsymbol{r}) \cdot \boldsymbol{p}(\boldsymbol{r}) \\ & + \frac{1}{3!}\int d\boldsymbol{r} \sum_{\alpha\beta\gamma\delta\rho\sigma} \frac{\partial\eta_\alpha}{\partial r_\beta}\frac{\partial\eta_\gamma}{\partial r_\delta}\frac{\partial\eta_\rho}{\partial r_\sigma} A_{\alpha\gamma\rho}^{\beta\delta\sigma} \\ & (\alpha, \beta, \gamma, \delta, \rho, \sigma = 1, 2, 3). \end{aligned} \tag{C1}$$

Here $\boldsymbol{\eta}$ is the atomic displacement from its equilibrium (different from index η in previous uses), $\boldsymbol{G}$ is the fourth rank tensor in Cartesian components representing the elastic moduli, $\mathfrak{D}_0$ is the equilibrium mass density of the material, and $\boldsymbol{A}$ is the sixth rank tensor of the third derivatives of the potential energy (anharmonic term). $\boldsymbol{p}$ and $\boldsymbol{\eta}$ are canonically conjugate if they refer to the same point in the medium, just as they would be if they referred to the same particle in the lattice.[38] Ziman assumes the commutation relations in the language of field theory as

$$[\boldsymbol{\eta}(\boldsymbol{r}), \boldsymbol{p}(\boldsymbol{r}')] = i\hbar\delta(\boldsymbol{r}' - \boldsymbol{r})\mathbf{I}, \tag{C2}$$

where $\delta(\boldsymbol{r}' - \boldsymbol{r})$ is the three-dimensional Dirac delta function. One can expand the operators $\boldsymbol{p}(\boldsymbol{r})$ and $\boldsymbol{\eta}(\boldsymbol{r})$ in Fourier series taking new operators $\boldsymbol{P_q}$ and $\boldsymbol{Q_q}$ as coefficients, i.e.,

$$\boldsymbol{\eta}(\boldsymbol{r}) = \frac{1}{\sqrt{V}}\sum_{\boldsymbol{q}} \boldsymbol{Q_q} e^{-i\boldsymbol{q}\cdot\boldsymbol{r}}, \quad \boldsymbol{p}(\boldsymbol{r}) = \frac{1}{\sqrt{V}}\sum_{\boldsymbol{q}} \boldsymbol{P_q} e^{i\boldsymbol{q}\cdot\boldsymbol{r}}. \tag{C3}$$

Then, Eq. (C1) can be transformed to

$$\begin{aligned} \mathcal{H} = & \frac{1}{2}\sum_{\boldsymbol{q}} \left\{ \sum_{\alpha\gamma} Q_{\boldsymbol{q}}^\alpha Q_{-\boldsymbol{q}}^\gamma \sum_{\beta\delta} q_\beta q_\delta G_{\alpha\gamma}^{\beta\delta} + \mathfrak{D}_0^{-1} \boldsymbol{P_q} \cdot \boldsymbol{P_{-q}} \right\} \\ & - \frac{i}{3!\sqrt{V}} \sum_{\boldsymbol{q},\boldsymbol{q}',\boldsymbol{q}''} \delta_{\boldsymbol{g},\boldsymbol{q}+\boldsymbol{q}'+\boldsymbol{q}''} \sum_{\alpha\gamma\rho} Q_{\boldsymbol{q}}^\alpha Q_{\boldsymbol{q}'}^\gamma Q_{\boldsymbol{q}''}^\rho \\ & \times \sum_{\beta\delta\sigma} q_\beta q'_\delta q''_\sigma A_{\alpha\gamma\rho}^{\beta\delta\sigma}. \end{aligned} \tag{C4}$$

To complete the quantum-mechanical description, some information about the eigenstates is needed. For this, Ziman returned to the operator formulation of Eq. (C4) and transformed to normal coordinate operators

$$\boldsymbol{Q_q} = \frac{1}{\sqrt{\mathfrak{D}_0}}\sum_p \boldsymbol{e}_{\boldsymbol{q},p} \mathbb{Q}_{\boldsymbol{q},p}, \quad \boldsymbol{P_q} = \sqrt{\mathfrak{D}_0}\sum_p \boldsymbol{e}_{\boldsymbol{q},p}^* \mathbb{P}_{\boldsymbol{q},p}, \tag{C5}$$

where $\boldsymbol{e}_{\boldsymbol{q},p}$ are the polarization vectors. One obtains the

Hamiltonian of an elastic continuum in the second quantization formalism as[38]

$$\begin{aligned}\mathcal{H} &= \frac{1}{2}\sum_{\boldsymbol{q},p}\left\{\mathbb{P}_{\boldsymbol{q},p}\mathbb{P}^{*}_{\boldsymbol{q},p} + \omega^{2}_{\boldsymbol{q},p}\mathbb{Q}_{\boldsymbol{q},p}\mathbb{Q}^{*}_{\boldsymbol{q},p}\right\} \\ &\quad - \frac{i}{3!\sqrt{V\mathfrak{D}_0^3}}\sum_{\boldsymbol{q},p;\boldsymbol{q}',p';\boldsymbol{q}'',p''}\delta_{\boldsymbol{g},\boldsymbol{q}+\boldsymbol{q}'+\boldsymbol{q}''}\mathbb{Q}_{\boldsymbol{q},p}\mathbb{Q}_{\boldsymbol{q}',p'}\mathbb{Q}_{\boldsymbol{q}'',p''} \\ &\quad \times \sum_{\alpha\beta\gamma\delta\rho\sigma}\boldsymbol{e}^{\alpha}_{\boldsymbol{q},p}\boldsymbol{e}^{\gamma}_{\boldsymbol{q}',p'}\boldsymbol{e}^{\rho}_{\boldsymbol{q}'',p''}q_\beta q'_\delta q''_\sigma A^{\beta\delta\sigma}_{\alpha\gamma\rho}, \\ \mathbb{P}_{\boldsymbol{q},p} &= \sqrt{\frac{\hbar\omega_{\boldsymbol{q},p}}{2}}\left(a_{\boldsymbol{q},p} + a^{*}_{-\boldsymbol{q},p}\right), \\ \mathbb{Q}_{\boldsymbol{q},p} &= -i\sqrt{\frac{\hbar}{2\omega_{\boldsymbol{q},p}}}\left(a^{*}_{\boldsymbol{q},p} - a_{-\boldsymbol{q},p}\right),\end{aligned} \tag{C6}$$

where $\omega_{\boldsymbol{q},p}$ is the phonon frequency at $\boldsymbol{q}$ and branch p, $a_{\boldsymbol{q},p}$ is the phonon annihilation operator, $a^{*}_{\boldsymbol{q},p}$ is the phonon creation operator, and $\boldsymbol{g}$ is the reciprocal lattice vector. One can now easily derive the relation between elastic moduli, anharmonicity, and Grüneisen parameter as

$$\gamma_{\boldsymbol{q},p} = -\frac{1}{6}\frac{\sum_{\alpha\beta\gamma\delta\rho}\boldsymbol{e}^{\alpha}_{\boldsymbol{q},p}\boldsymbol{e}^{\gamma}_{\boldsymbol{q},p}q_\beta q_\delta A^{\beta\delta\rho}_{\alpha\gamma\rho}}{\sum_{\alpha\beta\gamma\delta}\boldsymbol{e}^{\alpha}_{\boldsymbol{q},p}\boldsymbol{e}^{\gamma}_{\boldsymbol{q},p}q_\beta q_\delta G^{\beta\delta}_{\alpha\gamma}}, \tag{C7}$$

where the denominator of Eq. (C7) is written as[38]

$$\sum_{\alpha\beta\gamma\delta}\boldsymbol{e}^{\alpha}_{\boldsymbol{q},p}\boldsymbol{e}^{\gamma}_{\boldsymbol{q},p}q_\beta q_\delta G^{\beta\delta}_{\alpha\gamma} = \mathfrak{D}_0\omega^{2}_{\boldsymbol{q},p}. \tag{C8}$$

Finally, from Eqs. (C7) and (C8), the relation

$$\sum_{\alpha\beta\gamma\delta\rho}\boldsymbol{e}^{\alpha}_{\boldsymbol{q},p}\boldsymbol{e}^{\gamma}_{\boldsymbol{q},p}q_\beta q_\delta A^{\beta\delta\rho}_{\alpha\gamma\rho} = -6\sqrt{\gamma_{\boldsymbol{q},p}\gamma_{-\boldsymbol{q},p}}\mathfrak{D}_0\omega^{2}_{\boldsymbol{q},p}, \tag{C9}$$

can be found. Here, $\gamma_{\boldsymbol{q},p}$ was replaced by $\sqrt{\gamma_{\boldsymbol{q},p}\gamma_{-\boldsymbol{q},p}}$ for later convenient use.

The cubic crystals with four-fold axes have only six types of independent coefficients A which are[38]

$$A^{111}_{111},\ A^{112}_{112},\ A^{123}_{123},\ A^{133}_{122},\ A^{122}_{111},\ A^{312}_{231}. \tag{C10}$$

If the central forces are used to derive the elastic energy, there are, in addition, the Cauchy relations[38]

$$A^{123}_{123} = A^{312}_{231} = A^{133}_{122}, A^{112}_{112} = A^{122}_{111}. \tag{C11}$$

In an isotropic solid, there are only three second-order elastic constants

$$A^{111}_{111},\ A^{112}_{112},\ A^{123}_{123} \tag{C12}$$

[the first three terms in Eq. (C10)], which enter Eq. (C9). In our model of the perturbation operator, (i) the local strain in x-direction (NW axis) is assumed to cancel out, (ii) the total volume of the NW with rough surface is assumed to be the same as that of the ideal NW, and (iii) the roughness in y-direction is indistinguishable from that in z-direction. Then, the following anharmonic terms survive

$$A^{yyz}_{yyz},\ A^{yzy}_{yzy},\ A^{zyy}_{zyy},\ A^{zzy}_{zzy},\ A^{zyz}_{zyz},\ A^{yzz}_{yzz}. \tag{C13}$$

Therefore, Eq. (C9) can be written as

$$\begin{aligned}&\sum_{\substack{\alpha,\rho=y,z\\ \alpha\neq\rho}}\boldsymbol{e}^{\alpha}_{\boldsymbol{q},p}\boldsymbol{e}^{\alpha}_{\boldsymbol{q},p}q_\alpha q_\alpha A^{\alpha\alpha\rho}_{\alpha\alpha\rho} + 2\sum_{\substack{\alpha,\rho=y,z\\ \alpha\neq\rho}}\boldsymbol{e}^{\alpha}_{\boldsymbol{q},p}\boldsymbol{e}^{\rho}_{\boldsymbol{q},p}q_\alpha q_\rho A^{\alpha\rho\alpha}_{\alpha\rho\alpha} \\ &\quad = -6\sqrt{\gamma_{\boldsymbol{q},p}\gamma_{-\boldsymbol{q},p}}\mathfrak{D}_0\omega^{2}_{\boldsymbol{q},p}.\end{aligned} \tag{C14}$$

The factor 2 comes from the symmetry relation $A^{\alpha\rho\alpha}_{\alpha\rho\alpha} = A^{\rho\alpha\alpha}_{\rho\alpha\alpha}$. Finally, Eq. (C14) is generalized to

$$\begin{aligned}&\sum_{\substack{\alpha,\rho=y,z\\ \alpha\neq\rho}}\boldsymbol{e}^{\alpha}_{\boldsymbol{q},p}\boldsymbol{e}^{\alpha}_{\boldsymbol{q},p'}q_\alpha q_\alpha A^{\alpha\alpha\rho}_{\alpha\alpha\rho} + 2\sum_{\substack{\alpha,\rho=y,z\\ \alpha\neq\rho}}\boldsymbol{e}^{\alpha}_{\boldsymbol{q},p}\boldsymbol{e}^{\rho}_{\boldsymbol{q},p'}q_\alpha q_\rho A^{\alpha\rho\alpha}_{\alpha\rho\alpha} \\ &\quad = -6\sqrt{\gamma_{\boldsymbol{q},p}\gamma_{-\boldsymbol{q},p'}}\mathfrak{D}_0\omega^{2}_{\boldsymbol{q},p},\end{aligned} \tag{C15}$$

which implies that the Grüneisen parameter also comprises transitions between different branches. Only the anharmonicity parameters appearing in Eq. (C15) are kept in the anharmonic potential of Eq. (C6). This results in the perturbing Hamiltonian

$$\begin{aligned}\mathcal{V}_{anh} &= -\frac{i}{3!\sqrt{V\mathfrak{D}_0^3}}\sum_{\boldsymbol{q},p;\boldsymbol{q}',p';\boldsymbol{q}'',p''}\delta_{\boldsymbol{g},\boldsymbol{q}+\boldsymbol{q}'+\boldsymbol{q}''}\mathbb{Q}_{\boldsymbol{q},p}\mathbb{Q}_{\boldsymbol{q}',p'}\mathbb{Q}_{\boldsymbol{q}'',p''} \\ &\quad \times\left(\sum_{\substack{\alpha,\rho=y,z\\ \alpha\neq\rho}}\boldsymbol{e}^{\alpha}_{\boldsymbol{q},p}\boldsymbol{e}^{\alpha}_{\boldsymbol{q}',p'}q_\alpha q'_\alpha A^{\alpha\alpha\rho}_{\alpha\alpha\rho}\boldsymbol{e}^{\rho}_{\boldsymbol{q}'',p''}q''_\rho\right. \\ &\quad \left.+2\sum_{\substack{\alpha,\rho=y,z\\ \alpha\neq\rho}}\boldsymbol{e}^{\alpha}_{\boldsymbol{q},p}\boldsymbol{e}^{\rho}_{\boldsymbol{q}',p'}q_\alpha q'_\rho A^{\alpha\rho\alpha}_{\alpha\rho\alpha}\boldsymbol{e}^{\alpha}_{\boldsymbol{q}'',p''}q''_\alpha\right).\end{aligned} \tag{C16}$$

Umklapp processes are neglected, i.e., $\boldsymbol{g} = 0$, in accordance with the theory of an elastic continuum (limit of small $|\boldsymbol{q}|$). In Eq. (C16), one can change $\boldsymbol{q}'$ to $-\boldsymbol{q}'$ under the sum which gives

$$\begin{aligned}\mathcal{V}_{anh} &= \frac{i}{3!\sqrt{V\mathfrak{D}_0^3}}\sum_{\boldsymbol{q},p;\boldsymbol{q}',p';p''}\mathbb{Q}_{\boldsymbol{q},p}\mathbb{Q}_{-\boldsymbol{q}',p'}\mathbb{Q}_{\boldsymbol{q}'-\boldsymbol{q},p''} \\ &\quad \times\left[\sum_{\substack{\alpha,\rho=y,z\\ \alpha\neq\rho}}\boldsymbol{e}^{\alpha}_{\boldsymbol{q},p}\boldsymbol{e}^{\alpha}_{-\boldsymbol{q}',p'}q_\alpha q'_\alpha A^{\alpha\alpha\rho}_{\alpha\alpha\rho}\boldsymbol{e}^{\rho}_{\boldsymbol{q}'-\boldsymbol{q},p''}\left(q'_\rho - q_\rho\right)\right. \\ &\quad \left.+2\sum_{\substack{\alpha,\rho=y,z\\ \alpha\neq\rho}}\boldsymbol{e}^{\alpha}_{\boldsymbol{q},p}\boldsymbol{e}^{\rho}_{-\boldsymbol{q}',p'}q_\alpha q'_\rho A^{\alpha\rho\alpha}_{\alpha\rho\alpha}\boldsymbol{e}^{\alpha}_{\boldsymbol{q}'-\boldsymbol{q},p''}\left(q'_\alpha - q_\alpha\right)\right].\end{aligned} \tag{C17}$$

From Eq. (C17), with

$$\mathbb{Q}^*_{\boldsymbol{q},p} = \mathbb{Q}_{-\boldsymbol{q},p},\ \sum_{p''} \boldsymbol{e}^{\rho}_{\boldsymbol{q}'',p''} q''_{\rho} \mathbb{Q}_{\boldsymbol{q}'',p''} = -i\frac{\sqrt{\mathfrak{D}_0}}{\sqrt{V}} \Lambda^{\rho}_{\boldsymbol{q}''},$$
$$\Lambda^{\rho}_{\boldsymbol{q}''} = \int d\boldsymbol{r} \frac{\partial \eta_{\rho}}{\partial r_{\rho}} e^{i\boldsymbol{q}''\cdot\boldsymbol{r}}, \tag{C18}$$

one finds

$$\mathcal{V}_{anh} = \frac{1}{3!V\mathfrak{D}_0} \sum_{\boldsymbol{q},p;\boldsymbol{q}',p'} \mathbb{Q}_{\boldsymbol{q},p}\mathbb{Q}^*_{\boldsymbol{q}',p'} \times \left(\sum_{\substack{\alpha,\rho=y,z \\ \alpha\neq\rho}} \boldsymbol{e}^{\alpha}_{\boldsymbol{q},p}\boldsymbol{e}^{\alpha}_{-\boldsymbol{q}',p'} q_{\alpha} q'_{\alpha} A^{\alpha\alpha\rho}_{\alpha\alpha\rho} \Lambda^{\rho}_{\boldsymbol{q}'-\boldsymbol{q}} + 2 \sum_{\substack{\alpha,\rho=y,z \\ \alpha\neq\rho}} \boldsymbol{e}^{\alpha}_{\boldsymbol{q},p}\boldsymbol{e}^{\rho}_{-\boldsymbol{q}',p'} q_{\alpha} q'_{\rho} A^{\alpha\rho\alpha}_{\alpha\rho\alpha} \Lambda^{\alpha}_{\boldsymbol{q}'-\boldsymbol{q}} \right). \tag{C19}$$

The roughness profiles in y- and z-direction are equivalent, and $L_y = L_z = d$, where d is the diameter of the NW. With the assumption of a uniform dilatation ($\frac{\partial \eta_y}{\partial y} = \frac{2\Delta(x,z)}{d} = \frac{\partial \eta_z}{\partial z} = \frac{2\Delta(x,y)}{d}$), it follows that $\Lambda^y_{\boldsymbol{q}} = \Lambda^z_{\boldsymbol{q}}$. The factor 2 arises because for a given Cartesian direction, the dilatation has its starting point at the center of the NW. Let us first consider the (x,y)-plane only in which a dilatation is oriented in z-direction ($\frac{\partial \eta_z}{\partial z} = \frac{2\Delta(x,y)}{d} = \frac{2\Delta(\boldsymbol{r}_{//,xy})}{d}$, $\boldsymbol{r}_{//,xy} = \boldsymbol{x} + \boldsymbol{y}$, and $\boldsymbol{r} = \boldsymbol{z} + \boldsymbol{r}_{//,xy}$). One can then write Eqs. (C15), (C18), and (C19) in the form

$$\boldsymbol{e}^{z}_{\boldsymbol{q},p}\boldsymbol{e}^{z}_{\boldsymbol{q},p'} q_z q_z A^{zzy}_{zzy} + 2\boldsymbol{e}^{y}_{\boldsymbol{q},p}\boldsymbol{e}^{z}_{\boldsymbol{q},p'} q_y q_z A^{yzy}_{yzy} = -3\sqrt{\gamma_{\boldsymbol{q},p}\gamma_{-\boldsymbol{q},p'}}\mathfrak{D}_0\omega^2_{\boldsymbol{q},p}, \tag{C20}$$

$$\Lambda^y_{\boldsymbol{q}''} = \Lambda^z_{\boldsymbol{q}''} = 2\int d^2\boldsymbol{r}_{//,xy}\Delta(\boldsymbol{r}_{//,xy}) e^{i\boldsymbol{q}''_{//}\cdot\boldsymbol{r}_{//,xy}} \delta_{q''_z,0}, \tag{C21}$$

$$\mathcal{V}_{anh,xy} = \frac{1}{3!V\mathfrak{D}_0} \sum_{\boldsymbol{q},p;\boldsymbol{q}',p'} \mathbb{Q}_{\boldsymbol{q},p}\mathbb{Q}^*_{\boldsymbol{q}',p'} \times \left(\boldsymbol{e}^{z}_{\boldsymbol{q},p}\boldsymbol{e}^{z}_{-\boldsymbol{q}',p'} q_z q'_z A^{zzy}_{zzy} + 2\boldsymbol{e}^{y}_{\boldsymbol{q},p}\boldsymbol{e}^{z}_{-\boldsymbol{q}',p'} q_y q'_z A^{yzy}_{yzy} \right) \Lambda^y_{\boldsymbol{q}'-\boldsymbol{q}}. \tag{C22}$$

Inserting Eq. (C21) to Eq. (C22), the expression for the perturbing potential becomes

$$\mathcal{V}_{anh,xy} = \frac{2}{3!V\mathfrak{D}_0} \sum_{\substack{\boldsymbol{q},p;\boldsymbol{q}',p' \\ q'_z = q_z}} \mathbb{Q}_{\boldsymbol{q},p}\mathbb{Q}^*_{\boldsymbol{q}',p'} \times \left(\boldsymbol{e}^{z}_{\boldsymbol{q},p}\boldsymbol{e}^{z}_{-\boldsymbol{q},p'} q_z q_z A^{zzy}_{zzy} + 2\boldsymbol{e}^{y}_{\boldsymbol{q},p}\boldsymbol{e}^{z}_{-\boldsymbol{q},p'} q_y q_z A^{yzy}_{yzy} \right) \times \int d^2\boldsymbol{r}_{//,xy}\Delta(\boldsymbol{r}_{//,xy}) e^{i\left(\boldsymbol{q}'_{//}-\boldsymbol{q}_{//}\right)\cdot\boldsymbol{r}_{//,xy}}. \tag{C23}$$

Replacing here the brace by Eq. (C20), one obtains

$$\mathcal{V}_{anh,xy} = -\frac{1}{V} \sum_{\boldsymbol{q},p;\boldsymbol{q}',p'} \mathbb{Q}_{\boldsymbol{q},p}\mathbb{Q}^*_{\boldsymbol{q}',p'} \sqrt{\gamma_{\boldsymbol{q},p}\gamma_{-\boldsymbol{q},p'}}\omega^2_{\boldsymbol{q},p} \times \int d^2\boldsymbol{r}_{//,xy}\Delta(\boldsymbol{r}_{//,xy}) e^{i\left(\boldsymbol{q}'_{//}-\boldsymbol{q}_{//}\right)\cdot\boldsymbol{r}_{//,xy}} \delta_{q'_z-q_z,0}. \tag{C24}$$

Since $q'_z = q_z$, one can replace $\boldsymbol{q}'_{//} - \boldsymbol{q}_{//}$ by $\boldsymbol{q}' - \boldsymbol{q}$ in the exponent. Therefore, Eq. (C24) can be written in the form

$$\mathcal{V}_{anh,xy} = -\frac{1}{V} \sum_{\boldsymbol{q},p;\boldsymbol{q}',p'} \mathbb{Q}_{\boldsymbol{q},p}\mathbb{Q}^*_{\boldsymbol{q}',p'} \sqrt{\gamma_{\boldsymbol{q},p}\gamma_{-\boldsymbol{q},p'}}\omega^2_{\boldsymbol{q},p} \times \int d^2\boldsymbol{r}_{//,xy}\Delta(\boldsymbol{r}_{//,xy}) e^{i(\boldsymbol{q}'-\boldsymbol{q})\cdot\boldsymbol{r}_{//,xy}} \delta_{q'_z-q_z,0}. \tag{C25}$$

Considering now a constant dilatation perpendicular to the (x,z)-plane, the same derivation leads to the contribution

$$\mathcal{V}_{anh,xz} = -\frac{1}{V} \sum_{\boldsymbol{q},p;\boldsymbol{q}',p'} \mathbb{Q}_{\boldsymbol{q},p}\mathbb{Q}^*_{\boldsymbol{q}',p'} \sqrt{\gamma_{\boldsymbol{q},p}\gamma_{-\boldsymbol{q},p'}}\omega^2_{\boldsymbol{q},p} \times \int d^2\boldsymbol{r}_{//,xz}\Delta(\boldsymbol{r}_{//,xz}) e^{i(\boldsymbol{q}'-\boldsymbol{q})\cdot\boldsymbol{r}_{//,xz}} \delta_{q'_y-q_y,0}\,, \tag{C26}$$

to the total perturbation. Here, the integral extends over the (x,z)-plane.

The Grüneisen parameter is assumed to be a constant number, γ. Since both planes must be included and their contributions are equal by symmetry, the perturbing potential finally becomes

$$\mathcal{V}_{anh} = -\frac{2\gamma}{V} \sum_{\boldsymbol{q},p;\boldsymbol{q}',p'} \mathbb{Q}_{\boldsymbol{q},p}\mathbb{Q}^*_{\boldsymbol{q}',p'} \omega^2_{\boldsymbol{q},p} \times \int d^2\boldsymbol{r}_{//,xy}\Delta(\boldsymbol{r}_{//,xy}) e^{i(\boldsymbol{q}'-\boldsymbol{q})\cdot\boldsymbol{r}_{//,xy}} \delta_{q'_z-q_z,0}. \tag{C27}$$

In the form of second quantization, one can write

$$\mathbb{Q}_{\boldsymbol{q},p}\mathbb{Q}^*_{\boldsymbol{q}',p'} = -\frac{\hbar}{2}\frac{1}{\sqrt{\omega_{\boldsymbol{q},p}\omega_{\boldsymbol{q}',p'}}} \times \left(a^*_{\boldsymbol{q},p}a^*_{-\boldsymbol{q}',p'} - a^*_{\boldsymbol{q},p}a_{\boldsymbol{q}',p'} - a_{-\boldsymbol{q},p}a^*_{-\boldsymbol{q}',p'} + a_{-\boldsymbol{q},p}a_{\boldsymbol{q}',p'} \right). \tag{C28}$$

The average rate of change of the phonon occupation number ($n_{\boldsymbol{q},p}$) is[56]

$$\left.\frac{dn_{\boldsymbol{q},p}}{dt}\right] = -\frac{n_{\boldsymbol{q},p} - \langle n_{\boldsymbol{q},p}\rangle}{\tau_{ph}},\ \langle n_{\boldsymbol{q},p}\rangle = \frac{1}{e^{\hbar\omega_{\boldsymbol{q},p}/k_BT} - 1}, \tag{C29}$$

where $\langle n_{\boldsymbol{q},p}\rangle$ is the Bose-Einstein distribution function and τ_{ph} is the phonon RT. The left-hand side of Eq. (C29) is equal to the sum over energy of the transition rate

$$\left.\frac{dn_{\boldsymbol{q},p}}{dt}\right] = \sum_f \wp(E_i; E_f),$$
$$\wp(E_i; E_f) = \frac{2\pi}{\hbar}\left|\langle E_i|H'|E_f\rangle\right|^2 \delta(E_f - E_i), \tag{C30}$$

where E_i ($|n_{\boldsymbol{q},p}, n_{\boldsymbol{q}',p'}\rangle$) is the energy of state i and H' is the perturbing Hamiltonian. E_f can be the energy of a phonon removed from mode $(\boldsymbol{q}, p)$ and created in mode $(\boldsymbol{q}', p')$ ($|E_f\rangle = |n_{\boldsymbol{q},p} - 1, n_{\boldsymbol{q}',p'} + 1\rangle$) or vice versa ($|E_f\rangle = |n_{\boldsymbol{q},p} + 1, n_{\boldsymbol{q}',p'} - 1\rangle$). Using this, Eqs. (C29) and (C30), and the

perturbing Hamiltonian derived in Eq. (C27) lead to the RT

$$\frac{1}{\tau_{\boldsymbol{q},p}} = \frac{\omega_{\boldsymbol{q},p}^2\gamma^2}{4\pi^2 V}\sum_{p'}\int_{\omega_{\boldsymbol{q}',p'}=\omega_{\boldsymbol{q},p}} \frac{dS'}{v_{ph}\left(\omega_{\boldsymbol{q}',p'}\right)} \times \left|\int d^2\boldsymbol{r}_{//,xy}\Delta\left(\boldsymbol{r}_{//,xy}\right)e^{i(\boldsymbol{q}'-\boldsymbol{q})\cdot\boldsymbol{r}_{//,xy}}\right|^2 \times \frac{n_{\boldsymbol{q},p}-\overline{n_{\boldsymbol{q}',p'}}}{n_{\boldsymbol{q},p}-\left\langle n_{\boldsymbol{q},p}\right\rangle}\delta_{q_z'-q_z,0}, \tag{C31}$$

where dS' is the area element of the energy surface integration, v_{ph} is the phonon group velocity, and $\overline{n_{\boldsymbol{q}',p'}}$ is a suitable average of $n_{\boldsymbol{q}',p'}$ which is equal to $\left\langle n_{\boldsymbol{q},p}\right\rangle$ for an isotropy solid. The latter will be used here.

The absolute square term in Eq. (C31) can be written as

$$\left|\int d^2\boldsymbol{r}_{//,xy}\Delta\left(\boldsymbol{r}_{//,xy}\right)e^{i(\boldsymbol{q}'-\boldsymbol{q})\cdot\boldsymbol{r}_{//,xy}}\right|^2 = L_x d\int d^2\boldsymbol{r}_{//,xy} \times \left\langle\Delta\left(\boldsymbol{r}'_{//,xy}\right)\Delta\left(\boldsymbol{r}'_{//,xy}-\boldsymbol{r}_{//,xy}\right)\right\rangle e^{-i(\boldsymbol{q}'-\boldsymbol{q})\cdot\boldsymbol{r}_{//,xy}}, \quad \frac{1}{L_x d}\int d^2\boldsymbol{r}'_{//,xy}\Delta\left(\boldsymbol{r}'_{//,xy}\right)\Delta\left(\boldsymbol{r}'_{//,xy}-\boldsymbol{r}_{//,xy}\right) = \left\langle\Delta\left(\boldsymbol{r}'_{//,xy}\right)\Delta\left(\boldsymbol{r}'_{//,xy}-\boldsymbol{r}_{//,xy}\right)\right\rangle. \tag{C32}$$

GA and EA functions are used in Eq. (C32) leading to

$$\left\langle\Delta\left(\boldsymbol{r}'_{//,xy}\right)\Delta\left(\boldsymbol{r}'_{//,xy}-\boldsymbol{r}_{//,xy}\right)\right\rangle = \begin{cases}\Delta^2 e^{-\boldsymbol{r}_{//,xy}^2/L^2} & \text{GA}\\ \Delta^2 e^{-|\boldsymbol{r}_{//,xy}|/L} & \text{EA}\end{cases}. \tag{C33}$$

The Fourier transform in Eq. (C33) with GA and EA functions takes the form

$$\left|\int d^2\boldsymbol{r}_{//,xy}\Delta\left(\boldsymbol{r}_{//,xy}\right)e^{i(\boldsymbol{q}'-\boldsymbol{q})\cdot\boldsymbol{r}_{//,xy}}\right|^2 = 2L_x d\pi\Delta^2 L^2\begin{cases}\frac{1}{2}e^{-|\boldsymbol{q}'-\boldsymbol{q}|^2L^2/4} & \text{GA}\\ \left(1+|\boldsymbol{q}'-\boldsymbol{q}|^2L^2\right)^{-3/2} & \text{EA}\end{cases}. \tag{C34}$$

Inserting Eq. (C34) into Eq. (C31), the RTs for SR scattering become

$$\frac{1}{\tau_{sr}^{\boldsymbol{q},p}} = \frac{\omega_{\boldsymbol{q},p}^2\gamma^2\Delta^2L^2}{2\pi d}\sum_{p'}\int_{\omega_{\boldsymbol{q}',p'}=\omega_{\boldsymbol{q},p}}\frac{dS'}{v_{ph}\left(\omega_{\boldsymbol{q}',p'}\right)} \begin{cases}\frac{1}{2}e^{-|\boldsymbol{q}'-\boldsymbol{q}|^2L^2/4}\delta_{q_z'-q_z,0} & \text{GA}\\ \left(1+|\boldsymbol{q}'-\boldsymbol{q}|^2L^2\right)^{-3/2}\delta_{q_z'-q_z,0} & \text{EA}\end{cases}. \tag{C35}$$

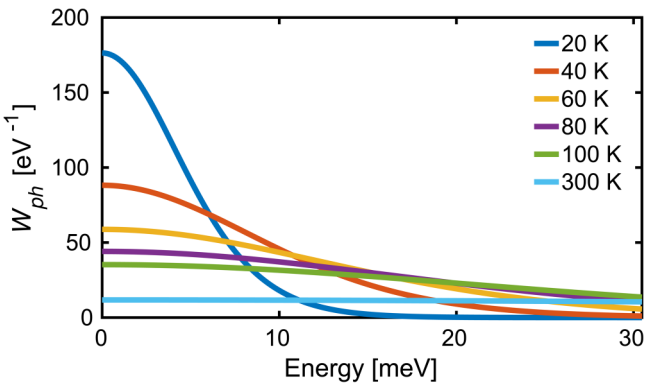

FIG. 15. Energy dependence of W_{ph} for different temperatures.

APPENDIX D: SIGNIFICANCE OF THE WINDOW FUNCTION

The phonon energies contributing to the thermal conduction can be described by the window function W_{ph}. At room temperature, W_{ph} is almost constant ($\sim$10 eV^{-1}) with a slightly decaying slope (Fig. 15). Therefore, the high-energy phonons cannot be ignored at T = 300 K, but their importance reduces at lower temperatures. Below 50 K, a peak at zero energy develops. The integral over $W_{ph}(E)$ is always equal to 1.

[1]G. J. Snyder and E. S. Toberer, Nat. Mater. **7**, 105 (2008).
[2]L.-D. Zhao, S.-H. Lo, Y. Zhang, H. Sun, G. Tan, C. Uher, C. Wolverton, V. P. Dravid, and M. G. Kanatzidis, Nature **508**, 373 (2014).
[3]A. I. Hochbaum, R. Chen, R. D. Delgado, W. Liang, E. C. Garnett, M. Najarian, A. Majumdar, and P. Yang, Nature **451**, 163 (2008).
[4]A. I. Boukai, Y. Bunimovich, J. Tahir-Kheli, J.-K. Yu, W. A. G. Iii, and J. R. Heath, Nature **451**, 168 (2008).
[5]S. F. Karg, V. Troncale, U. Drechsler, P. Mensch, P. D. Kanungo, H. Schmid, V. Schmidt, L. Gignac, H. Riel, and B. Gotsmann, Nanotechnology **25**, 305702 (2014).
[6]J. P. Heremans, V. Jovovic, E. S. Toberer, A. Saramat, K. Kurosaki, A. Charoenphakdee, S. Yamanaka, and G. J. Snyder, Science **321**, 554 (2008).
[7]Y. Pei, X. Shi, A. LaLonde, H. Wang, L. Chen, and G. J. Snyder, Nature **473**, 66 (2011).
[8]Y. Pei, A. LaLonde, S. Iwanaga, and G. J. Snyder, Energy Environ. Sci. **4**, 2085 (2011).
[9]Q. Zhang, B. Liao, Y. Lan, K. Lukas, W. Liu, K. Esfarjani, C. Opeil, D. Broido, G. Chen, and Z. Ren, Proc. Natl. Acad. Sci. U.S.A. **110**, 13261 (2013).
[10]Q. Zhang, E. K. Chere, K. McEnaney, M. Yao, F. Cao, Y. Ni, S. Chen, C. Opeil, G. Chen, and Z. Ren, Adv. Energy Mater. **5**, 1401977 (2015).
[11]L.-D. Zhao, G. Tan, S. Hao, J. He, Y. Pei, H. Chi, H. Wang, S. Gong, H. Xu, V. P. Dravid, C. Uher, G. J. Snyder, C. Wolverton, and M. G. Kanatzidis, Science **351**, 141 (2016).
[12]N. Mingo, D. Hauser, N. P. Kobayashi, M. Plissonnier, and A. Shakouri, Nano Lett. **9**, 711 (2009).
[13]K. Biswas, J. He, Q. Zhang, G. Wang, C. Uher, V. P. Dravid, and M. G. Kanatzidis, Nat. Chem. **3**, 160 (2011).
[14]B. Liao, B. Qiu, J. Zhou, S. Huberman, K. Esfarjani, and G. Chen, Phys. Rev. Lett. **114**, 115901 (2015).
[15]B. Liao, A. A. Maznev, K. A. Nelson, and G. Chen, Nat. Commun. **7**, 13174 (2016).
[16]P. Caroff, K. A. Dick, J. Johansson, M. E. Messing, K. Deppert, and L. Samuelson, Nat. Nanotechnol. **4**, 50 (2009).
[17]R. E. Algra, M. A. Verheijen, M. T. Borgstrm, L.-F. Feiner, G. Immink, W. J. P. v. Enckevort, E. Vlieg, and E. P. A. M. Bakkers, Nature **456**, 369 (2008).
[18]H. J. Joyce, Q. Gao, H. H. Tan, C. Jagadish, Y. Kim, X. Zhang, Y. Guo, and J. Zou, Nano Lett. **7**, 921 (2007).
[19]A. Mishra, L. V. Titova, T. B. Hoang, H. E. Jackson, L. M. Smith, J. M. Yarrison-Rice, Y. Kim, H. J. Joyce, Q. Gao, H. H. Tan, and C. Jagadish, Appl. Phys. Lett. **91**, 263104 (2007).
[20]J. Bao, D. C. Bell, F. Capasso, J. B. Wagner, T. Mrtensson, J. Trgrdh, and L. Samuelson, Nano Lett. **8**, 836 (2008).
[21]N. Akopian, G. Patriarche, L. Liu, J.-C. Harmand, and V. Zwiller, Nano Lett. **10**, 1198 (2010).
[22]T. Ba Hoang, A. F. Moses, L. Ahtapodov, H. Zhou, D. L. Dheeraj, A. T. J. van Helvoort, B.-O. Fimland, and H. Weman, Nano Lett. **10**, 2927 (2010).

[23]T. Kouno, M. Sakai, K. Kishino, and K. Hara, Jpn. J. Appl. Phys. **53**, 068001 (2014).
[24]S. Castelletto, Z. Bodrog, A. P. Magyar, A. Gentle, A. Gali, and I. Aharonovich, Nanoscale **6**, 10027 (2014).
[25]K. P. Korona, A. Reszka, M. Sobanska, P. S. Perkowska, A. Wysmoek, K. Klosek, and Z. R. Zytkiewicz, J. Lumin. **155**, 293 (2014).
[26]P. Corfdir, C. Hauswald, J. K. Zettler, T. Flissikowski, J. Lahnemann, S. Fernandez-Garrido, L. Geelhaar, H. T. Grahn, and O. Brandt, Phys. Rev. B **90**, 195309 (2014).
[27]Y. Li, Z. Liu, X. Lu, Z. Su, Y. Wang, R. Liu, D. Wang, J. Jian, J. H. Lee, H. Wang, Q. Yu, and J. Bao, Nanoscale **7**, 1601 (2015).
[28]J. A. d. Alamo, Nature **479**, 317 (2011).
[29]N. Waldron, S. Sioncke, J. Franco, L. Nyns, A. Vais, X. Zhou, H. C. Lin, G. Boccardi, J. W. Maes, Q. Xie, M. Givens, F. Tang, X. Jiang, E. Chiu, A. Opdebeeck, C. Merckling, F. Sebaai, D. v. Dorp, L. Teugels, A. S. Hernandez, K. D. Meyer, K. Barla, N. Collaert, and Y. V. Thean, in *2015 IEEE International Electron Devices Meeting (IEDM)* (IEEE, 2015), pp. 31.1.1–31.1.4
[30]H. Schmid, M. Borg, K. Moselund, L. Gignac, C. M. Breslin, J. Bruley, D. Cutaia, and H. Riel, Appl. Phys. Lett. **106**, 233101 (2015).
[31]R. Rhyner and M. Luisier, Nano Lett. **16**, 1022 (2016).
[32]J. Lim, K. Hippalgaonkar, S. C. Andrews, A. Majumdar, and P. Yang, Nano Lett. **12**, 2475 (2012).
[33]G. Kresse and J. Furthmuller, Phys. Rev. B **54**, 11169 (1996).
[34]J. P. Perdew, A. Ruzsinszky, G. I. Csonka, O. A. Vydrov, G. E. Scuseria, L. A. Constantin, X. Zhou, and K. Burke, Phys. Rev. Lett. **100**, 136406 (2008).
[35]N. S. Orlova, Phys. Stat. Sol. (b) **119**, 541 (1983).
[36]K. Vuttivorakulchai, M. Luisier, and A. Schenk, in *2016 International Conference on Simulation of Semiconductor Processes and Devices (SISPAD)* (IEEE, 2016), pp. 19–22.
[37]C. Jeong, S. Datta, and M. Lundstrom, J. Appl. Phys. **111**, 093708 (2012).
[38]J. M. Ziman, *Electrons and Phonons: The Theory of Transport Phenomena in Solids*, Oxford Classic Texts in the Physical Sciences (Oxford University Press, New York, 2001).
[39]M. G. Holland, Phys. Rev. **132**, 2461 (1963).
[40]D. T. Morelli, J. P. Heremans, and G. A. Slack, Phys. Rev. B **66**, 195304 (2002).
[41]A. D. Stuckes, Phil. Mag. **5**, 84 (1960).
[42]R. Bowers, R. W. Ure, J. E. Bauerle, and A. J. Cornish, J. Appl. Phys. **30**, 930 (1959).
[43]P. V. Tamarin and S. S. Shalyt, Sov. Phys. Semicond. **5**, 1097 (1971).
[44]F. Zhou, A. L. Moore, J. Bolinsson, A. Persson, L. Froberg, M. T. Pettes, H. Kong, L. Rabenberg, P. Caroff, D. A. Stewart, N. Mingo, K. A. Dick, L. Samuelson, H. Linke, and L. Shi, Phys. Rev. B **83**, 205416 (2011).
[45]A. F. Mayadas, M. Shatzkes, and J. F. Janak, Appl. Phys. Lett. **14**, 345 (1969).
[46]A. Y. Serov, Z.-Y. Ong, and E. Pop, Appl. Phys. Lett. **102**, 033104 (2013).
[47]C. Toher, J. J. Plata, O. Levy, M. de Jong, M. Asta, M. B. Nardelli, and S. Curtarolo, Phys. Rev. B **90**, 174107 (2014).
[48]P. Martin, Z. Aksamija, E. Pop, and U. Ravaioli, Phys. Rev. Lett. **102**, 125503 (2009).
[49]G. Kresse and D. Joubert, Phys. Rev. B **59**, 1758 (1999).
[50]P. E. Blöchl, Phys. Rev. B **50**, 17953 (1994).
[51]H. J. Monkhorst and J. D. Pack, Phys. Rev. B **13**, 5188 (1976).
[52]A. Paul, M. Luisier, and G. Klimeck, J. Comput. Electron. **9**, 160 (2010).
[53]S. Steiger, M. Salmani-Jelodar, D. Areshkin, A. Paul, T. Kubis, M. Povolotskyi, H.-H. Park, and G. Klimeck, Phys. Rev. B **84**, 155204 (2011).
[54]A. A. Maradudin, E. W. Montroll, and G. H. Weiss, *Theory of Lattice Dynamics in the Harmonic Approximation*, Solid State Physics, Supplement 3 (Academic Press, New York, 1963).
[55]K. Parlinski, Z. Q. Li, and Y. Kawazoe, Phys. Rev. Lett. **78**, 4063 (1997).
[56]P. G. Klemens, in *Solid State Physics*, edited by F. Seitz and D. Turnbull (Academic Press, 1958), Vol. 7, pp. 1–98.